Applied Geochemistry 80 (2017) 112–133

Contents lists available at ScienceDirect

Applied Geochemistry

journal homepage: www.elsevier.com/locate/apgeochem

Geochemistry of metals and metalloids in siliceous sinter deposits: Implications for elemental partitioning into silica phases

Camilo Sanchez-Yanez*, Martin Reich, Mathieu Leisen, Diego Morata, Fernando Barra

Department of Geology and Andean Geothermal Center of Excellence (CEGA), Universidad de Chile, Plaza Ercilla, 803, Santiago, Chile

ARTICLE INFO

Article history:
Received 12 October 2016
Received in revised form
1 March 2017
Accepted 13 March 2017
Available online 23 March 2017

Editorial handling by Prof. M. Kersten.

Keywords:
Puchuldiza
Altiplano
High-altitude
Siliceous sinter
Silica crystallinity
Precious metals
Metalloids
Nanoparticle
Ostwald ripening

ABSTRACT

Sinter deposits are formed by precipitation of silica from hydrothermal fluids that have reached the surface environment. They are commonly found around hot springs and represent surface expressions of underlying geothermal systems and/or low sulfidation epithermal gold-silver hydrothermal deposits. Several studies have reported ppm to weight percent concentrations of metals (e.g., Au, Ag, Cu) and metalloids (e.g., As, Sb, B) in sinters capping geothermal systems and epithermal gold-silver deposits. However, the relation between the maturity of the siliceous sinter and its metal enrichment remains unknown. Here we use geochemical and mineralogical data that link the silica crystallinity degree with trace metal and metalloid contents in sinter. In this paper, we provide in situ trace element data in metal-rich silica sinter samples from the Puchuldiza geothermal field in the Altiplano of northern Chile that record the complete diagenetic sequence from non-crystalline opal A to microcrystalline quartz. Combined SEM, XRD and LA-ICP-MS data show that the concentration of metals and metalloids in sinters from Puchuldiza display a strong correspondence with silica crystallinity. While arsenic and boron are predominantly enriched in the more amorphous silica phases (opal A/CT), gold and silver show higher concentrations in the more crystalline phases (opal C/quartz). Silica structural, morphological and geochemical transformations from its initial precipitation to its final maturation after diagenesis are responsible for this differential enrichment. During the initial stages, gold and silver are incorporated into silica microspheres as cationic species and/or metal nanoparticles or colloids, while arsenic and boron incorporation is controlled by As-bearing accessory minerals and Fe-oxyhydroxides. As diagenesis progresses and the crystallinity of silica increases, diffusion-driven processes such as Ostwald ripening may progressively enrich gold and silver in the sinter, while metalloids are depleted owing to the low retention of arsenic by silica. These findings indicate that the diagenetic transitions of silica, defined by significant structural changes that involve generation of surface defects and the creation of reactive sites, may play an important role in elemental uptake by silica in near surface environments.

1. Introduction

Siliceous sinters (or sinters) are natural chemical sedimentary deposits formed at or near the surface by precipitation from silica-rich, near neutral hydrothermal fluids as they discharge and cool at the surface (Fournier and Rowe, 1966; Rodgers et al., 2004; Lynne et al., 2007). Sinter deposits are commonly found around hot springs and represent surface expressions of underlying geothermal systems and/or low sulfidation, epithermal gold-silver deposits (Parker and Nicholson, 1990; Guido et al., 2002; Rodgers et al., 2004; Lynne et al., 2007; Sillitoe, 2015). Since sinter deposits form above the water table and close to the surface, they are commonly used to identify the paleoenvironmental conditions of extinct hot spring systems (Lynne et al., 2008). Furthermore, the identification and geomorphic interpretation of these paleosurface products can be used as guides for the exploration of concealed geothermal resources and epithermal precious metal deposits (Parker and Nicholson, 1990; Guido et al., 2002; Rodgers et al., 2004; Lynne et al., 2007; Sillitoe, 2015). Additionally, recent studies on silica sinter deposits have revealed preservation pathways of environmentally controlled, microbe-dominated sedimentary facies and biosignatures that are relevant to astrobiological investigation (Konhauser et al., 2001, 2003; Handley et al., 2005; Gibson et al., 2014; Campbell et al., 2015).

* Corresponding author.
E-mail address: casanche@ing.uchile.cl (C. Sanchez-Yanez).

http://dx.doi.org/10.1016/j.apgeochem.2017.03.008
0883-2927/

Sinter deposits are texturally complex and are predominantly composed of metastable silica phases (SiO_2*nH_2O) that include amorphous opal A, para-crystalline opal CT, opal C, and stable microcrystals of silica (SiO_2) including quartz and moganite (Smith, 1998; Rodgers et al., 2004; Lynne et al., 2007). In geothermal hot springs, silica precipitation is strongly controlled by the undercooling of thermal water, evaporation rate, and changes in the pH and ionic strength of the hydrothermal fluid (Ichikuni, 1970; Rimstidt and Cole, 1983; Campbell et al., 2003; Rodgers et al., 2004; Tobler et al., 2008; Tobler and Benning, 2013; Nicolau et al., 2014). The first stage of sinter formation comprises the nucleation of $Si(OH)_4$ monomers in the silica-saturated fluid. This promotes aggregation by coagulation and/or floculation of colloidal silica particles, with coarser grains formed by Ostwald ripening (Iler, 1979; Smith, 1998; Tobler et al., 2008, 2009; Tobler and Benning, 2013). The first silica phases precipitated from the hydrothermal fluid have very low structural order and their morphologies result from aggregations of porous nano- to micro-sized silica spheres (Rodgers et al., 2004; Lynne et al., 2007). Silica undergoes further morphological and structural transitions as a result of changes in the thermodynamic conditions, such as variable exposure to weathering, fluid re-circulation, and changes in the degree of silica saturation, temperature, pH, and evaporation rate, among others (Williams et al., 1985; Herdianita et al., 2000a; Konhauser et al., 2001; Lynne and Campbell, 2004; Rodgers et al., 2004; Nicolau et al., 2014). Each silica phase displays particular morphologies as expressions of their internal structure. A higher structural order or maturation grade is reached during diagenesis as a result of increased density and a decrease in porosity and water content (Herdianita et al., 2000a; Rodgers et al., 2004; Lynne et al., 2008).

Several recent mineralogical studies have focused on the texture, morphology, degree of crystallinity, and biogeochemical signatures of silica sinters (e.g., Herdianita et al., 2000a; Rodgers et al., 2004; Fernandez-Turiel et al., 2005; Lynne et al., 2007; Garcia-Valles et al., 2008; Lynne, 2012b; Orange et al., 2013; Tobler and Benning, 2013; Nicolau et al., 2014), whereas other studies have centered on the presence of metals and metalloids in sinters that form common accessory minerals in low sulfidation gold-silver epithermal deposits (Ichikuni, 1970; Parker and Nicholson, 1990; Saunders, 1990; McKenzie et al., 2001; Guido et al., 2002; Guidry and Chafetz, 2003; Pope et al., 2005; Sillitoe, 2015). Common accesory minerals reported in different sinter deposits include, pyrite, stibnite, realgar, orpiment, and cinnabar. Additionally, amorphous arsenic and antimony sulfides have been identified in the Waiotapu sinter, New Zealand (Jones et al., 2001), and halite, sylvite, realgar, gypsum and cahnite have been reported at the El Tatio sinter deposits, in northern Chile (Nicolau et al., 2014). Sinter deposits can contain several elements at the ppm level (i.e., Au, Ag, Li, B, As, Mo, Hg, Cu, Pb, Sb, and W). In the Waiotapu geothermal field, New Zealand, reported gold and silver values range from 9.2 to 543 ppm and 3.7–33 ppm, respectively (Pope et al., 2005; Jones et al., 2001). Guido et al. (2002) have documented 18–530 ppm of Ag and 3.8–8.1 ppm of Cu in paleo sinters from the El Deseado massif, Argentina, and Uysal et al. (2011) have shown that sinter samples from the Drummond Basin in Queensland, Australia, have up to 7.98 ppm of Cu. Besides these data, no studies have combined the sinter trace element geochemistry with the silica crystallinity degree. This is critical in order to determine the possible mineralogical controls on the abundance of trace metals in the sinter. Further, there is no published information regarding the form of these metals in the sinter, i.e., structurally bound into particular silica phases, or if they are incorporated as nano- to micro-sized mineral particles into sinter. This information is not only relevant to evaluate the partition of dissolved metal species into silica phases during sinter formation, but it is also crucial to better understand metal transport and precipitation in near surface hydrothermal systems, and to assess the potential impacts of silica precipitation on toxic metal uptake and release in the local environment.

This study provides new in situ trace element data in natural silica sinter samples that record the complete diagenetic sequence from non-crystalline opal A to microcrystalline quartz. The metal-rich silica sinter samples were obtained in the Puchuldiza geothermal field located in the Altiplano of northern Chile. This active geothermal system has been previously evaluated for high-enthalpy geothermal resources and as a potential epithermal gold-silver prospect (JICA, 1979). The purpose of this study is to determine the relation between the degree of silica crystallinity, the micro-morphology and the trace metal/metalloid content. We use a combination of techniques including scanning electron microscopy (SEM) observations, X-ray diffraction (XRD) structural characterization and laser-ablation inductively-coupled plasma mass spectrometry (LA-ICP-MS).

The high-altitude (>4.000 m a.s.l) silica sinter deposits of the Chilean Altiplano exhibit unique textural and mineralogical characteristics resulting from the extreme climatic conditions. These include a high degree of structural disorder, which is probably related to cation incorporation into the silica structure and/or the occurrence of micro- to nano-scale accessory minerals (Garcia-Valles et al., 2008; Nicolau et al., 2014). Our data indicates that the degree of silica crystallinity plays a fundamental role in the metal and metalloid uptake in geothermal systems.

2. Geological background and samples

The Puchuldiza geothermal field is located in the Altiplano Plateau of northern Chile (19.412925°S, 68.959900°W) at an elevation of 4200 m above sea level (m a.s.l.), and 200 km east of the city of Iquique, Tarapacá region (Fig. 1). The geothermal field covers an area of ~1 km^2 (Fig. 2A) and the sinter deposits occur in a volcano-tectonic depression that is structurally controlled by a NW-SE reverse fault system and a NNE-SSW normal – strike-slip fault system (Lahsen et al., 2005; Tassi et al., 2010; Amberg, 2011). The geology of the area is represented by a Cretaceous continental sequence overlain by Miocene to Pliocene andesitic and dacitic lavas. Ash-flow tuffs, and glacial and alluvial deposits of Holocene age cover an important part of the area (Lahsen, 1970; Lahsen et al., 2005). The hydrothermal surface alteration in the geothermal area is characterized by typical low sulfidation alteration assemblages, that is mainly sericite and adularia (JICA, 1979).

The Puchuldiza field has more than 100 surface expressions of geothermal activity that are related to the intersection of the fault systems described above. The area comprises an extensive paleo-sinter deposit (Fig. 2 C,E), actively forming siliceous sinters (Fig. 2F and G) and surface manifestations including hot, bubbling and thermal springs, fumaroles, geysers and mud pools (Fig. 2 B,-D). The near boiling (87.6 °C at ~4.200 m a.s.l.) spring waters are characterized by a near-neutral pH and are rich in alkalis and chloride (alkali-chloride type). Previous geothermometry determinations indicate a geothermal reservoir temperature at depth in the range of 180° to 240 °C (JICA, 1979; Mahon and Cusicanqui, 1980; Lahsen et al., 2005).

The silica sinter deposits in Puchuldiza have an estimated thickness of up to 25 m according to previous geophysical prospecting (Ortiz et al., 2008) and exhibit textures related to fast to intermittent flow of hot water. Siliceous sinters are characterized by different colorations that form bands, nodules or surface precipitates (Fig. 2 C,-E,-F,-G), probably related to changes in their chemical content and the incorporation of bio-materials such as

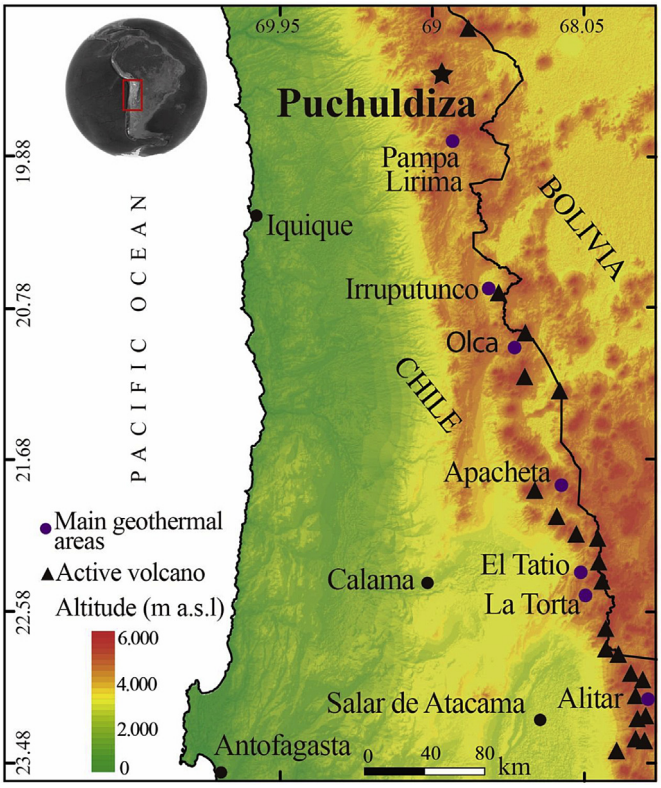

Fig. 1. Main Geothermal areas of northern Chile: Location map of the Puchuldiza geothermal field in the Altiplano of northern Chile. Other geothermal areas are shown (purple circles), as well as active volcanoes (black triangles). Figure modified from Nicolau et al. (2014) and Aravena et al. (2016). (For interpretation of the references to colour in this figure legend, the reader is referred to the web version of this article.)

thermophilic cyanobacteria and micro-algae (Schultze-Lam et al., 1995; Jones et al., 1999; Benning et al., 2005; Fernandez-Turiel et al., 2005; Gibson et al., 2008; Barbieri et al., 2014).

Thirteen silica sinter deposit associated with active and inactive geothermal manifestations were selected for sampling based on their coloration and textures (Fig. 2A). The sinters were deposited on pool margins (Fig. 2B), and discharge channels (Fig. 2 D), with mature phases in deep pool and proximal vent facies. Textures such as geyseritic, lily-pad, palisade and streamer (Guidry and Chafetz, 2003; Lynne, 2012b) were recognized in various samples containing different silica phases. In active vents, the sinter samples were collected in both subaqueous and subaerial settings. All sinter samples exhibited significant color variations in bands 0.2–0.5 cm wide. For each sample, fragments of consecutive bands were extracted to determine their mineralogy, crystallinity, micromorphology and geochemical characteristics. Additionally, water samples were collected for chemical analysis and the pH of the water were measured on site.

3. Analytical methods

Representative thirty-seven siliceous sinter samples were collected and analyzed using X-ray powder diffraction (XRD) methods as a means of identifying microcrystalline silica phases and accessory minerals according to established protocols (Smith, 1998; Herdianita et al., 2000b; Lynne et al., 2007; Nicolau et al., 2014). The XRD analyses were carried out using a Siemens D-5000 diffractometer in the Physics Department at the Universidad de Chile, Santiago. The untreated powder samples (<200 μm) were scanned at a rate of 0.6°2Θ/min, with a step size of 0.01°, from 0 to 80°2Θ, and operating conditions of 40 kV and 30 mA. Accessory minerals were identified using the XPowder12 software. In all diffractograms, the value of the Full Width at Half Maximum (FWHM) was measured by fitting the curve and base line manually (Lynne et al., 2007). The FWHM is the main parameter used to determine the degree of structural disorder in different non-crystalline silica (Smith, 1998; Lynne et al., 2007). This parameter was then used to assess the mineralogical maturation of silica and compared with other FWHM values from different silica sinter deposits worldwide.

The samples analyzed by XRD were also studied by scanning electron microscopy (SEM) in order to determine the morphological characteristics of silica and the presence of accessory minerals. Clean silica sinter samples were coated with a thin carbon film, and later mounted on a sample holder with carbon tape. The analyses were performed at the Andean Geothermal Centre of Excellence (CEGA), Universidad de Chile, using a FEI Quanta 250 SEM equipped with secondary electron (SE), energy-dispersive X-ray spectrometry (EDS), backscattered electron (BSE) and cathodoluminescence (CL) detectors. The analyses were performed using a spot size of 1–3 μm, an accelerating voltage of 10–20 keV, a beam intensity of 80 μA, and a working distance of 10 mm.

Semi-quantitative EDS analyses were used to constrain major elements in individual mineral phases. The EDS operating conditions were 20 keV, a spot size of 1–3 μm and a working distance of 10–18 mm.

Eight representative sinter samples previously studied under the SEM and structurally-characterized by XRD were selected for major and trace element analyses in specific silica sinter phases (opal A, opal A/CT, opal CT, opal CT/C and opal C/quartz). The measurements were carried out in the Isotope Geochemistry Laboratory at CEGA, Universidad de Chile, using a Thermo Scientific™ iCAP™ quadrupole inductively coupled plasma mass spectrometer (Q-ICP-MS) coupled with a 193 nm ArF excimer laser (Photon Machines Analyte G2). The following isotopes were analyzed: ^{7}Li, ^{11}B, ^{23}Na, ^{24}Mg, ^{27}Al, ^{39}K, ^{44}Ca, ^{48}Ti, ^{54}Fe, ^{55}Mn, ^{63}Cu, ^{75}As, ^{79}Br, ^{107}Ag, ^{121}Sb, and ^{197}Au. The ICP-MS operates with a RF power of 1550 W and a vacuum pump with a capacity of $<1 \times 10^{9}$ l/min with an acquisition time of 1.049 s for one cycle. Ablation was performed within a HelEx 2 cell, with two different spot sizes (20 and 30 μm) according to the grain size of silica in the samples. A repetition rate of 7 Hz and a constant fluency of 4.64 J/cm^2 were used with a 0.3 L/min flow of He as carrier gas. The calibration was performed using NIST 610 and 612 standards (National Institute of Standards and Technology). The samples were analyzed using a standard-sample-standard bracketing methodology. An Excel macro was developed for off-line data reduction. The data considered representative displayed a signal that is three times higher than the standard deviation of the background. Elemental quantification was carried out based on the normalization of the sum of all metal oxides to 100 wt.%. and the use of an ablation yield correction factor (AYCF) (Liu et al., 2008).

The concept behind this methodology can be developed as follows (equations (1)–(6))

$$C^{i}_{sam} = C^{i}_{rm} \times \left(\frac{cps^{i}_{sam}}{cps^{i}_{rm}}\right) \times \left\{\left(\frac{cps^{is}_{rm}}{cps^{is}_{sam}}\right) \times \left(\frac{C^{is}_{sam}}{C^{is}_{rm}}\right)\right\} \quad (1)$$

where C^{i}_{sam} represents the concentration of *i* element in the sample, and C^{i}_{rm} the concentration of element "*i*" in the reference material. The cps^{i}_{sam} and cps^{i}_{rm} are net count rates of analyzed element "*i*" in

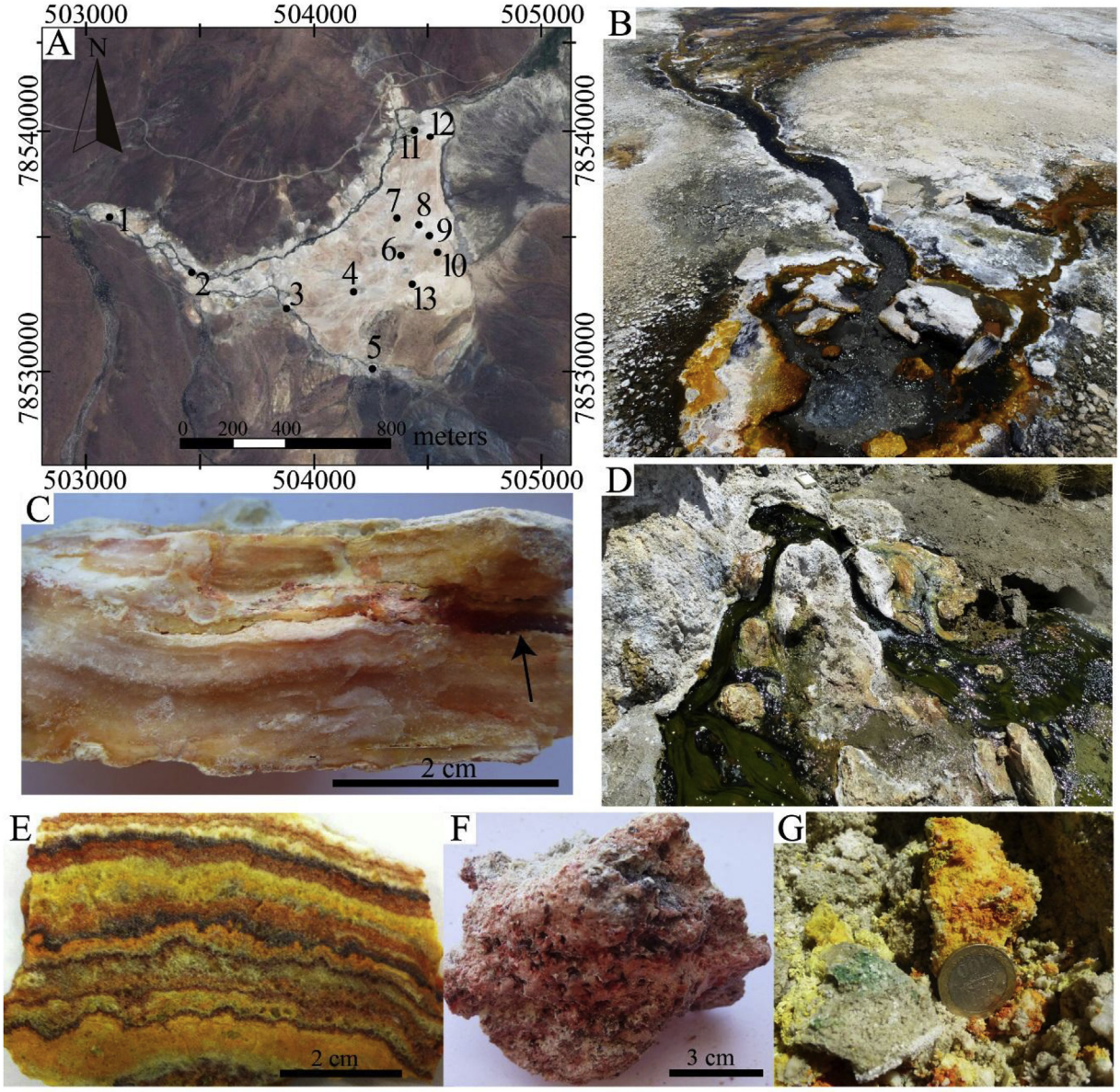

Fig. 2. Sampling sites and silica sinter samples: (A) Location of the 13 sinter sampling sites, distributed throughout the Puchuldiza field. Sites 8, 9 and 13 represent paleo-sinter and other sites are actively-forming sinter. (B and D) Sites 7 and 2 respectively. Sampling sites actively forming sinter related to bubbling pools. The pool in B has ~1 m diameter and in D the pool has ~0.3 m diameter, with discharge channels and temperatures of 84 °C and 54 °C, correspondingly. (C and E) Paleo-sinter samples showing multiple color bands and red nodules (black arrow in C), sampling site 9 and 13 respectively. (F and G): Active sinter samples showing high porosity (site 6, F) and nodules of a sulfide precipitate (site 11, G). (For interpretation of the references to colour in this figure legend, the reader is referred to the web version of this article.)

the sample and reference material, respectively, while cps^{is}_{rm} and cps^{is}_{sam} are net count rates of internal standard of element "*is*" in the sample. The C^{is}_{sam} and C^{is}_{rm} are the concentrations of "*is*" in the sample and in reference material, respectively (Liu et al., 2008). Considering that:

$$k = \left(\frac{cps^{is}_{rm}}{cps^{is}_{sam}}\right) \times \left(\frac{C^{is}_{sam}}{C^{is}_{rm}}\right) \tag{2}$$

the concentration of an element *i* in the sample is denoted by

$$C^{i}_{sam} = C^{i}_{rm} \times \left(\frac{cps^{i}_{sam}}{cps^{i}_{rm}}\right) \times k \tag{3}$$

Based on the fact that the sum of all elements is represented by 100 wt%, the concentration of all species in the sample can be expressed as:

$$\left(\sum_{i=1}^{N} C^{i}_{sam} \times \frac{C^{i}_{rm}}{cps^{i}_{rm}}\right) \times k = 100 \tag{4}$$

where *N* is the total number of elements in the sample and the value $\left(\frac{C^{i}_{rm}}{cps^{i}_{rm}}\right)$ can be calculated through regression statistics considering the analysis of reference materials, independently of an internal standard (Liu et al., 2008). The calculation of *k* represents a unique value and is denoted as the ablation yield correction factor (AYCF):

$$AYCF = \frac{100}{\sum_{j=1}^{N}\left[cps^{j}_{sam} \times \left(\frac{C^{i}_{rm}}{cps^{i}_{rm}}\right)\right]} \quad (5)$$

Finally, the concentration of each element (C^{is}_{sam}) in the samples is calculated using:

$$C^{i}_{sam} = AYCF \times cps^{i}_{sam} \times I^{i} \quad (6)$$

In addition to the mineralogical and trace element data of sinter samples, the chemical composition of nine geothermal spring water samples spatially associated with active sinter was determined. Separate samples for cations and anions were collected and filtered through a 0.45 μm cellulose acetate filter and stored in pre-cleaned polypropylene bottles. Samples for major cations and trace metal analyses were acidified with 4 N HNO_3. The samples were analyzed at the Fluid Geochemistry Laboratory at CEGA, Universidad de Chile, using atomic absorption spectrometry (AAS) for major cations, and ion chromatography (IC) for anions and bicarbonates. The trace element concentration of the geothermal water samples was analyzed using high resolution inductively coupled plasma – mass spectrometry (HR-ICP-MS) at Activation Laboratories Ltd (Actlabs), Canada.

4. Results

4.1. Sinter mineralogy and micro-morphology

The main mineralogical characteristics of the 37 sinter samples from Puchuldiza are listed in Table 1, including silica phases and accessory minerals. The FWHM value is also shown for each sample. Samples were classified as opal A, opal A/CT, opal CT, opal CT/C, and opal C/quartz according to their FWHM values and micro-morphologies (Lynne et al., 2007). Representative XRD traces for selected samples are shown in Fig. 3.

Active and fossil silica sinter samples from Puchuldiza exhibit a wide range of FWHM values from amorphous to crystalline phases, between 0.11°2Θ and 9.52°2Θ (Table 1). Samples M1.2, M3.2a, P8a, M3.5v, and M3.1a show the highest FWHM values and correspond to amorphous opal A. Samples with FWHM values higher than 7°2Θ were classified as the same phase (e.g., samples M3.1, M3.6, M3.3r, P7a). FWHM values between 0.39°2Θ and 6.59°2Θ were measured in samples P7d, M3.7B, M3.5, M3.6b, M3.6d, M2.6b, P5, M2.2b, M2.2r, M2.5b, and M2.5. In these samples, opal A/CT (4.3°2Θ - 6.59°2Θ), opal CT (1.6°2Θ - 2.51°2Θ), and opal CT/C (0.39°2Θ - 1.21°2Θ) phases were identified (Table 1). The most mature phases opal C/quartz were identified in samples M2.6r, M2.1, P1a and P1b, and show FWHM values of 0.11°2Θ - 0.28°2Θ.

The mineralogical contents and micro-morphologies are described for sinter samples as classified based on their constituent

Table 1
Mineralogical features of silica sinters from Puchuldiza. The FWHM values and the corresponding structural classification are provided, along with a general macroscopic description and location information. Accessory mineralogy is described for each sample.

Sample ID	FWHM (°2Θ)	Silica phase	Other constituents
M1.2	9.5	Opal A	Detrital quartz and hematite. Pool margin from actively-forming sinter site 4.
M3.2a	8.9	Opal A	Hematite, calcite, halite, and organic material. Pool margin from actively-forming sinter site 2.
P8a	8.5	Opal A	Laminated paleo-sinter from site 13, Sample of yellow bands (Fig. 2 E).
M3.5v	8.5	Opal A	Halite and silica microspheres encrusted on microorganisms filaments; from actively-forming sinter site 10.
M3.1a	8.3	Opal A	Halite and microorganisms. Pool margin from actively-forming sinter site 1.
M3.1ar	8.3	Opal A	Realgar, sulfur, halite and microorganisms. Sample from actively-forming sinter site 1.
M3.3	8.3	Opal A	Halite. From pool margin in actively-forming sinter mound, Site 3.
M3.1	8.2	Opal A	Quartz, anorthite, halite and microorganisms. Sample from actively-forming sinter site 1.
P8b	7.9	Opal A	Laminated paleo-sinter from site 13, Sample of brown bands (Fig. 2 E).
P7b	7.9	Opal A	Laminated paleo-sinter from site 13, Sample of red bands (Fig. 2 E).
M3.7v	7.7	Opal A	Calcite, albite, halite, quartz and organic matter. Site 11, actively-forming sinter.
P7e	7.7	Opal A	Laminated paleo-sinter, dark bands (Fig. 2 E). Site 13.
M3.1.r	7.5	Opal A	Halite in pool margin. Actively-forming sinter site 1.
P7a	7.7	Opal A	Laminated paleo-sinter, orange bands (Fig. 2 E). Site 13.
P7c	7.7	Opal A	Laminated paleo-sinter, white bands (Fig. 2 E). Site 13
M3.7	7.5	Opal A	Calcite. Site 11, actively-forming sinter.
M2.7m	7.5	Opal A	Sample from site 5, actively-forming sinter site
M3.3r	7.5	Opal A	Sample from site 3 with organic matter. Actively-forming sinter site
M3.6	7.5	Opal A	Halite. Sample from site 12, actively-forming sinter.
P8c	7.2	Opal A	Laminated paleo-sinter from site 13 (Fig. 2 E). Red-pink bands.
M3.7p	7.2	Opal A	Halite, hematite, magnetite and organic matter. Site 11, actively-forming sinter.
M3.1	7	Opal A	Realgar, halite and high presence of microorganisms. Site 1, actively-forming sinter.
P7d	6.5	Opal A/CT	Laminated paleo-sinter with white-brown bands (Fig. 2 E). Site 13.
M3.7b	5.6	Opal A/CT	Sample from site 11, actively-forming sinter.
M3.5	4.3	Opal A/CT	Quartz and halite. Sample from site 10, actively-forming sinter
M3.6b	2.5	Opal CT	Diffractogram with tridymite-like peaks, from site 12 actively-forming sinter.
M3.6d	2.5	Opal CT	Diffractogram with tridymite-like peaks and quartz, from site 12 actively-forming sinter.
M2.6b	1.9	Opal CT	Cinnabar, halite and cristobalite-like peaks. Site 6, actively-forming sinter.
P5	1.7	Opal CT	Paleo-sinter sample from site 13.
M2.2b	1.6	Opal CT	Cinnabar, halite and tridymite-like peaks. Laminated paleo-sinter in site 8, with white bands.
M2.2r	1.6	Opal CT	Cinnabar, halite and tridymite-like peaks. Laminated paleo-sinter in site 8, with red bands.
M2.5b	1.2	Opal CT/C	Calcite, quartz and cristobalite-like peaks. Site 7, actively-forming sinter site
M2.5	0.3	Opal CT/C	Quartz, cinnabar and cristobalite-like peaks. Site 7, actively-forming sinter site
M2.6r	0.2	Opal C/Quartz	Quartz, cinnabar and cristobalite-like peaks. Site 6, actively-forming sinter site
M2.1	0.2	Opal C/Quartz	Quartz. Site 9, Paleo sinter.
P1a	0.1	Opal C/Quartz	Quartz. Laminated paleo-sinter from site 13, with dark red bands.
P1b	0.1	Opal C/Quartz	Quartz. Laminated paleo-sinter from site 13, white-red bands.

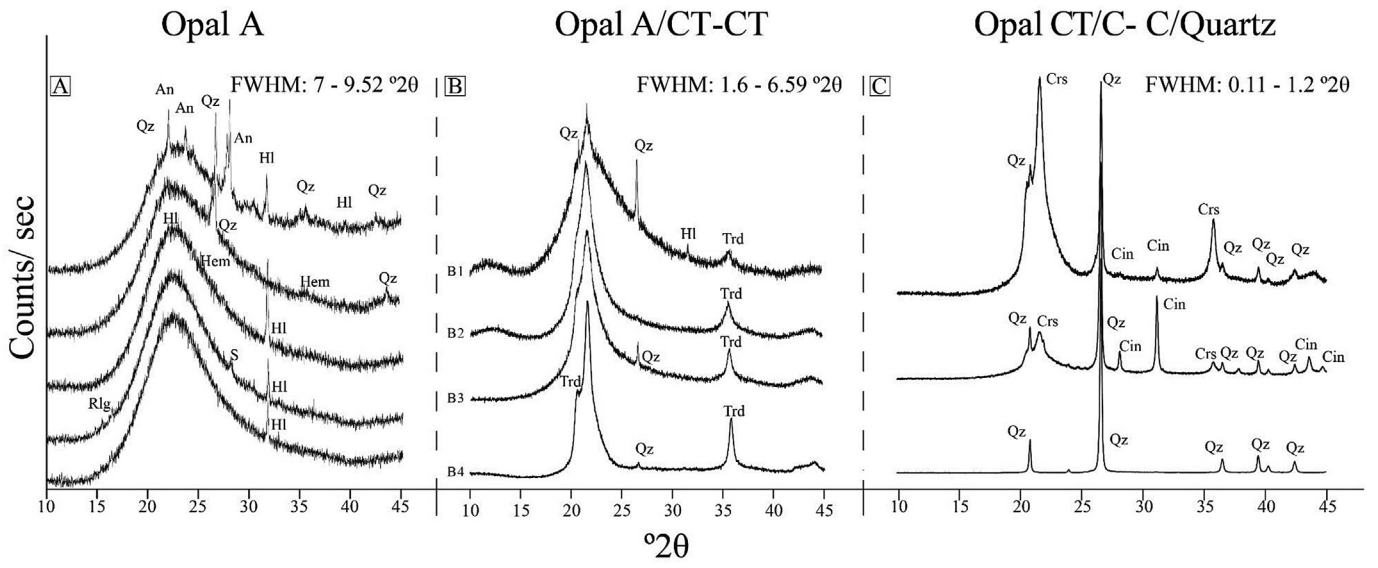

Fig. 3. Representative X-ray diffractogram traces of sinter samples from Puchuldiza: (A) Stack of 5 diffractograms of opal A- bearing samples: the broadband is centered at 23.5°2Θ -24 °2Θ, with FWHM values between 7°2Θ - and -9.5°2Θ. Samples top-down: M3.1, M1.2, M3.7p, M3.1ar, and M3.1a. (B) Stack of 4 diffractograms of paracrystalline silica phases: B1 correspond to opal A/CT, and B2, B3 and B4 to opal CT. The broadband in centered at ~21.5°2Θ, and FWHM values vary between 1.6 and 6.59°2Θ. Samples M3.5, M3.6b, M3.6D, P5. (C) Stack of 3 diffractograms of opal CT/C-C/quartz: the well-defined peaks of quartz are representative of high degree of crystallinity. Samples: M2.5, M2.6r, M2.1. Main accessory minerals phases are labeled and correspond to anorthite (An), hematite (Hem), realgar (Rlg), halite (Hl), detrital quartz (Qz), cinnabar (Cin), native sulphur (S), trydimite (Trd) and cristobalite (Crd).

silica phases (opal A, opal A/CT, opal CT, opal CT/C, and opal C/quartz). The Puchuldiza sinter samples are characterized by silica-bearing bands of variable coloration (e.g., Fig. 2 C,-E,-F,-G), although chemically pure silica is colorless (Rossman, 1994). The coloration is caused by chemical impurities in the silica and accessory minerals that co-precipitate with silica in sinter. The XRD patterns (Fig. 3 and Table 1) show halite (NaCl) as a common accessory mineral in all phases, and in amorphous and paracrystalline phases, detrital quartz was identified. Opal A phase-bearing samples (Fig. 3) contain hematite (Fe_2O_3) and magnetite (Fe_3O_4) in grey-red bands (samples M1.2, M3.2a, and M3.3r, M3.7p). Additionally, yellow-orange bands show realgar (As_4S_4) and native sulfur (e.g., samples M3.1, M3.1r and M3.1ar), while the pink coloration of sample M3.3r is related to orpiment (As_2S_3). The white color in opal A phases coincide with the presence of calcite ($CaCO_3$) and detrital quartz (samples M3.2a, M3.7 and M3.7a), even though some samples only display XRD patterns associated to amorphous silica. Opal A/CT phase-bearing samples show yellow and white coloration with only halite and detrital quartz as accessory minerals (e.g., in sample M3.5, opal A/CT-CT in Fig. 3). Opal CT, opal CT/C, and opal C/quartz-bearing samples (Fig. 3) display red, pink and yellow colors related to the co-existence of cinnabar (HgS) and halite (e.g., samples M2.6b, M2.2b, M2.2r, and M2.5). Some samples do not show accessory minerals as determined by XRD analyses, (e.g., M2.7m and P7c), although their coloration varies from white to different shades of white-pink, yellow, green, and red. This color variation is attributed mainly to chemical impurities or nano-scale mineral inclusions in silica that were not detected by XRD techniques.

The micro-morphologies observed in sinter samples from Puchuldiza are highly variable and strongly correlate with the degree of crystallinity. Samples containing amorphous and paracrystalline silica phases display microspheres with variable sizes in different distributions. For example, opal A-bearing samples (22 samples) exhibit well-defined microspheres with diameters between 1 and 6 μm and smooth surfaces. The microspheres in these samples are distributed in honeycomb (Fig. 4A), conglomerate and micro-botryoidal arrangements (Fig. 4B, -C); also, microspheres, occur on the surfaces of tubular microorganisms, forming smooth and rough filaments of ~10 and ~5 μm diameter, respectively (Figs. 4D and 5B). The presence of tubular microorganisms with different sizes is likely related with variation in the temperature of water (Fig. 5B). The filaments form a crisscross growth pattern without alignment resulting in a high porosity texture in the samples (e.g., samples M3.7b and M3.5v, Figs. 4D and 5B). Additionally, the silica microspheres are joined side by side or are interconnected in the botroydal arrangements filling the voids between filaments (Fig. 4D). In general, the silica microspheres exhibit a regular diameter in different samples (~1–6 μm), except for sample M1.2 which shows a coexistence of microspheres of variable sizes (<1–5 μm), that are related to different formations stages (Fig. 4C). Samples M3.1ar, M2.7m, M3.1m, and M3.3 show platelets <5 μm that are distributed homogeneously in the samples and are intergrown with silica microspheres (Fig. 5D, -C). SEM-EDS analyses suggest that platelets are composed of silica and show regular hexagonal shapes. Additionally, samples M2.7m, M3.1, and M3.3 show a massive vitreous silica matrix between silica microspheres or as massive bands (Fig. 5D); related to water evaporation (Rodgers et al., 2004). Microorganisms such as diatoms and microalgae were observed only in active sinter samples containing opal A silica. The microorganisms are usually associated with different aggregation of microspheres and in some cases they preserve their morphological characteristics (Fig. 5A), while in other cases tubular microorganisms are covered by silica microspheres (Figs. 4D and 5B).

Samples containing opal A/CT (samples P7d, M3.7b, and M3.5 in Table 1) display agglomeration of irregular microspheres of ~6–15 μm of diameter with rough surfaces and multiple clusters of filaments (Fig. 5B). For example, sample M3.7b shows a high porosity due to multiple filaments in a crisscross arrangement

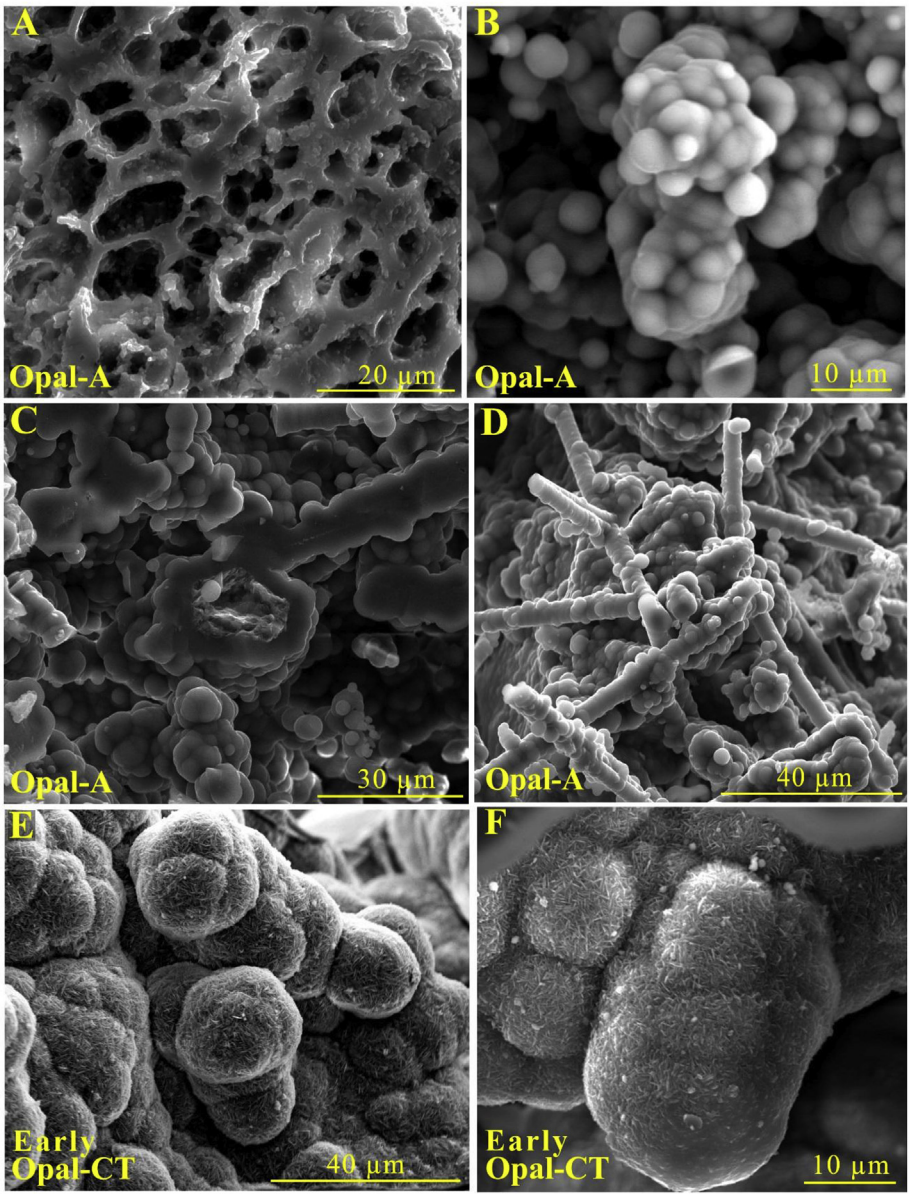

Fig. 4. Morphology and micro-textures of amorphous and semi-crystalline silica phases in sinters from Puchuldiza. (A) Opal A microspheres (1–4 μm) forming a honeycomb arrangement. Sample M3.5v. (B) Micro-botroidal arrangement of opal A microspheres of diameter ~4–5 μm. Sample P8a. (C) Clusters and packs of aligned opal A microspheres (2–6 μm), showing a fracture surface. Sample M1.2. (D) Opal A microspheres aligned in tubular rows as filaments. Sample M3.2a. (E) Agglomeration of early opal-CT microspheres ~6–15 μm diameter, showing lepispheres with roughness surfaces. Sample M3.6b. (F) Early Opal-CT lepispheres and micro-particles encrusted between silica platelets on larger microspheres. Sample M3.6d.

along with microspheres of ~10 μm and irregular silica platelets of 5–20 μm, both recognized in the voids generated by inter-filaments gaps. Additionally, samples containing opal CT (samples M3.6b, M3.6d, M2.6b, P5, M2.2b, and M2.2r) and opal CT/C (samples M2.5b and M2.5) exhibit agglomerations of uniform silica spheres of 10–25 μm of diameter (Fig. 4E, -F, and Fig. 6A, -B), with roughness to lepi-surfaces along with silica platelets <10 μm that occur side by side with silica spheres. In sample M2.2r, micro-silica platelets <5 μm were observed with silica microspheres <1 μm, both on the surfaces of lepispheres. The presence of these micro silica spheres is most likely associated with late-stage silica precipitation or colloidal transport in the hot water (Fig. 4F).

Sinter samples that contain the most mature silica phases (samples M2.6r, M2.1, P1a, P1b) show agglomeration of spheres of ~40–120 μm diameter with irregular surfaces. These irregular surfaces are formed by proto-crystals of quartz with sizes <10 μm, (Fig. 6C, -D), and well-developed microcrystals of quartz (10–30 μm) (Fig. 6E, -F). In sample M2.1, on the other hand, the micro-crystals were recognized mostly in micro-fractures and cavities within the sample. Well-developed quartz crystals usually occur inside voids, and do not show specific growth orientation.

Despite the fact that accessory minerals were detected by XRD (Table 1), the SEM inspection of samples did not allow a precise determination of their morphology, suggesting that these mineral species might be present as submicron-sized inclusions and/or are covered by layers of silica spheres or vitreous silica. The only exception is halite, which occurs as cubic crystals of 5–10 μm size in samples M2.5 and M3.1.

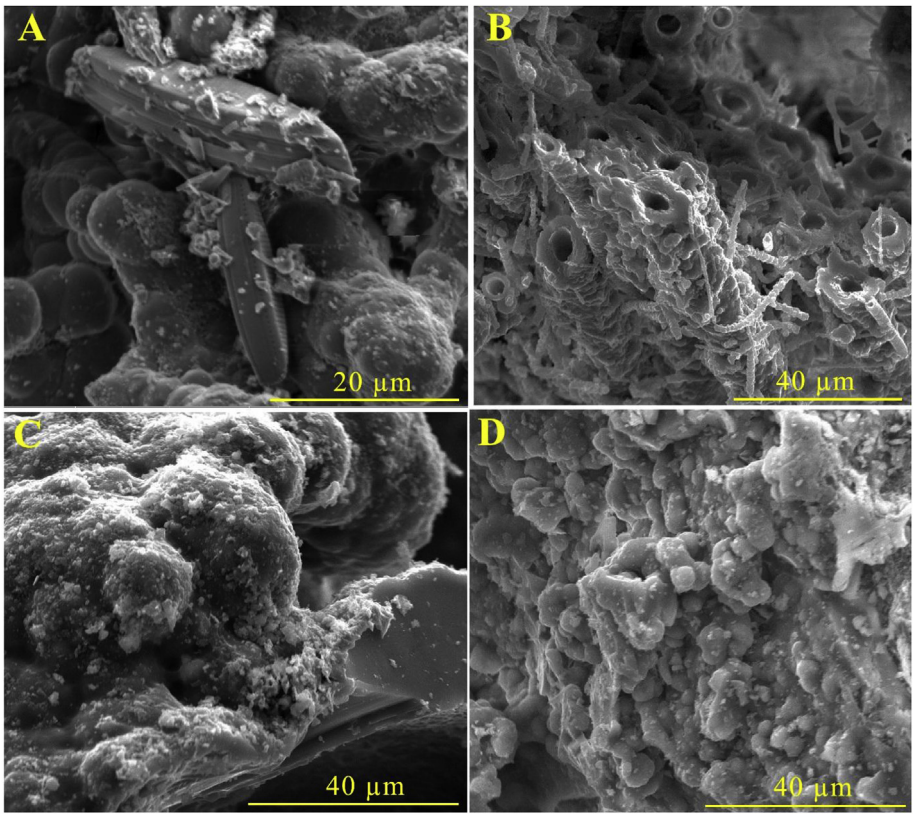

Fig. 5. Morphology and micro-textures and microbial components of the Puchuldiza sinters: (A) Diatoms between microspheres of opal A show well-defined forms and display silica platelets on their surfaces. Sample M3.1a. (B) Tubular microorganisms with microspheres of opal A encrusted on the surface. Sample M3.5v. (C) Microspheres show rough surfaces due to large amounts of silica platelets. An amorphous silica band can be observed at the bottom. Sample M2.6b. (D) Microspheres and silica platelets form clusters of different sizes. Sample M3.7p.

4.2. Sinter geochemistry and hydrothermal fluid composition

Representative LA-ICP-MS analyses of sinter samples from Puchuldiza are shown in Table 2, based on their degree of silica crystallinity, i.e., opal A, opal CT and opal C/quartz (samples analyses are presented in the Appendix). Sinter samples contain in average, more than 79.55 wt.% SiO_2, reaching a maximum of 95.82 wt.% in sample M3.7. CaO, Al_2O_3, Na_2O, K_2O, and Fe_2O_3 are present in all sinter samples and some MnO (samples M3.7, M3.6, M2.5 and M3.1) and MgO (samples M3.7, M3.6, and M2.5) were measured, some of these chemical species are present as accessories mineral such as calcite (ex. Samples M3.7 and M2.5b) and hematite (ex: samples M1.2 and M3.7p). The concentrations of CaO vary in average between 1.3 and 12.76 wt.%, with the highest value measured in sample M2.5. The Al_2O_3 show an average concentrations in the range of 0.043–1.186 wt.%, for samples M2.2r and M2.5, respectively. Na_2O is present in average, between 0.118 wt.% and 1.137% wt.% and shows little variation, similarly to K_2O which is present in an average concentrations of 0.102–0.454 wt.% in samples M3.1 and M2.5, respectively. Fe_2O_3 content was determined using ^{57}Fe, and show average values between 0.163 wt.% in sample M3.1 and 6.509 wt.% in sample M3.9b. MnO and MgO show average concentrations between 79.5 ppm to 473 ppm and 52.23–148 ppm, respectively.

Sinter samples contain high concentrations of metals and metalloids including Au, Ag, Cu, As, Sb, B and Li (Table 2). The less crystalline, more immature opal A-bearing sample M3.7 contains 0.29 ppm Au, 0.85 ppm Ag, and 21.63 ppm Cu as representative concentrations. The other elements are present with a wide range of representative concentrations in this silica phase, in samples M3.1 and M3.7, i.e., As (19090.25 ppm and 133.51 ppm), Sb (336.57–1007.24 ppm), B (24.37–83.45 ppm), and Li (1100.36–3015.65 ppm). Samples M3.6b is intermediate and less immature opal CT-bearing and contains a higher content of precious metals (10.3 ppm Au, 14.96 ppm Ag as representative values), and Cu (49.32 ppm). As, Sb, B and Li are present in relatively high concentrations (4233.93 ppm, 274.03 ppm, 87.85 ppm, 411.41 ppm, representatives values respectively). The most mature and crystalline opal C/quartz-bearing samples (samples M2.2r, M2.5, M2.5b, M2.6r, and M2.6b) show the highest concentrations of Au (1.86–30.58 ppm in samples M2.5b and M2.5), and Ag (9.3–111.98 ppm in samples M2.5 and M2.6b), whereas the other elements show variable concentrations (As: 18.63–662.64 ppm in samples M2.6r and M2.5, Sb: 270.69 ppm in M2.6r and 1568.4 ppm in M2.5b, B: 196.05–286.06 ppm in samples M2.5 and M2.6 respectively, Cu: 1.18 ppm in M2.6r and 157.26 ppm in M2.5, and Li 71.66–1213.55 ppm in samples M2.2r and M2.5 respectively).

In Fig. 7, the mean and median concentrations of Au, Ag, Cu, As, Sb, and B are plotted as a function of silica crystallinity. In addition, a compilation of previously published LA-ICP-MS analyses from other sinter deposits around the world is shown as a reference; however, no silica crystallinity was reported for these data, unless specified otherwise. These results reveal a significant correspondence between trace element concentrations and the degree of silica crystallinity. Gold and Ag show a trend of higher contents with increasing crystallinity, spanning two orders of magnitude in

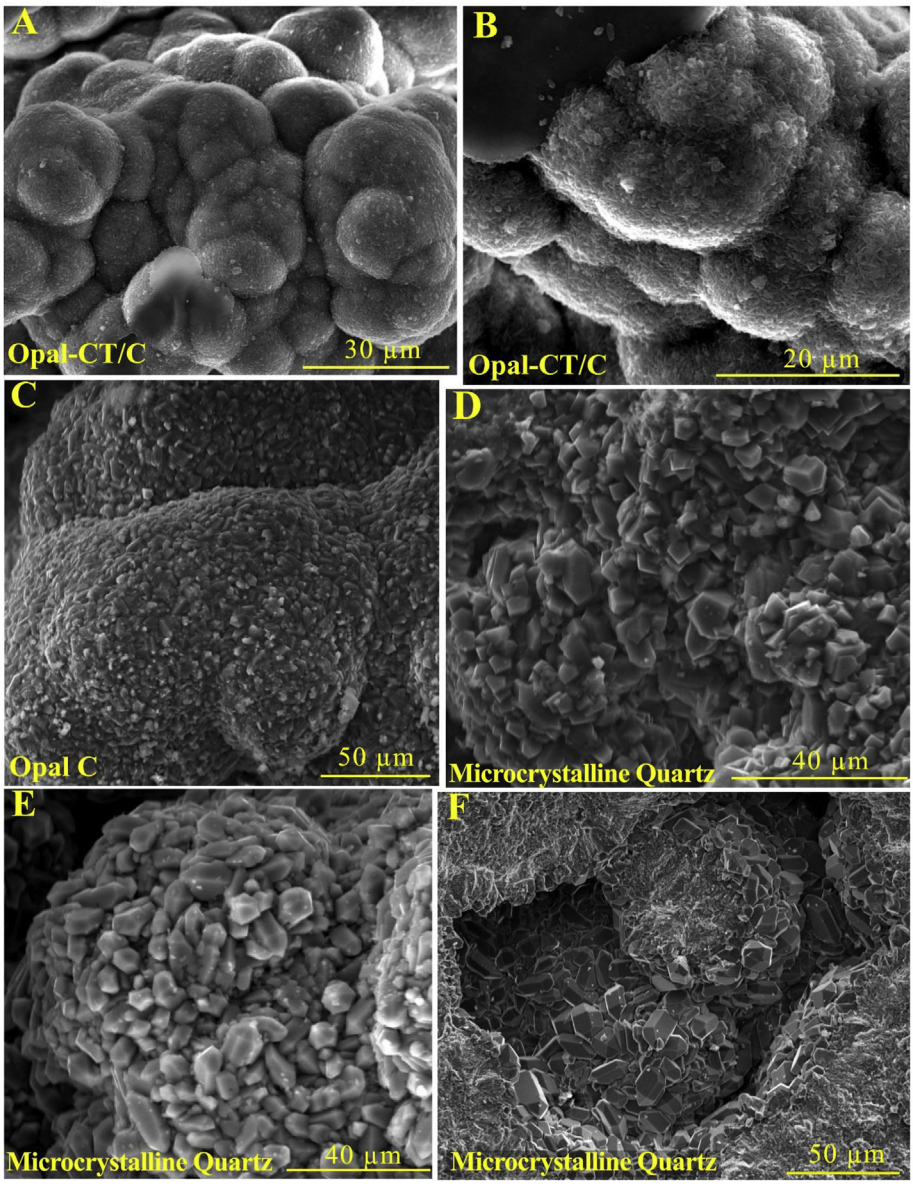

Fig. 6. Morphology and micro-textures of the more crystalline silica phases in sinters from Puchuldiza: (A) Agglomeration of opal C microspheres with rough surfaces. SampleM2.6b. (B) Agglomerated microspheres of opal-CT/C with quartz pseudo-microcrystals on the surface. Sample 2.5. (C) Typical morphology of opal C microspheres in sinter. Sample M2.6r. (D) Quartz microcrystals with prismatic faces. Sample M2.1. (E) Microcrystals of quartz on the surface of a microsphere. Sample P1a. (F) Well-defined bipyramidal microcrystals of quartz. Sample M2.1.

concentration from opal A to opal C/quartz. In contrast, As and B content show an inverse relationship with silica crystallinity. Finally, the concentration of other species such as Sb and Cu do not show a clear trend with the crystallinity degree of silica, and their median values do not vary distinctly between different silica phases (Fig. 7).

The geothermal water related to the sinter deposits are NaCl-dominated with temperatures ranging between 54.4 and 87.8 °C (the latter is the boiling T° at ~4.200 m a.s.l.), and pH varies between 6.2 and 8.8. The total dissolved solids (TDS) ranges from 4000 to 4500 mg/l, above the average of 3770 mg/l in geothermal springs from northern Chile (Tassi et al., 2010). Representative chemical analyses of major cations, anions and trace elements are shown in Table 3. The major constituents are SiO_2 (226.75–400.03 mg/l), Cl (2316–2616 mg/l), Na (1405–1625 mg/l), and K (144–218 mg/l), with B (73.9–88.6 mg/l), As (11–13 mg/l), and Li (10.6–12.9 mg/l) showing significant concentrations. Hg (0.0399–0.1 mg/l), Sb (0.0288–0.91 mg/l), and Cu (6.94–18.4 µg/l) also show high concentrations, and Au is present in low but measurable amounts (<1.8 ng/l) (Table 3).

5. Discussion

5.1. Silica precipitation and diagenetic maturation effects on trace element uptake

The siliceous sinter deposits at Puchuldiza record the complete diagenetic sequence from non-crystalline opal A to microcrystalline

Table 2
Selected trace element analyses of different silica phases determined by LA-ICP-MS. Concentration are in ppm unless specified otherwise (n.d.: not detected).

		Silica phases							
		Opal A		Opal CT	Opal C/quartz				
		M3.1	M3.7	M3.6b	M2.2r	M2.5	M2.5b	M2.6b	M2.6r
SiO_2 (wt%)	min	85.62	93.95	70.30	88.56	69.60	64.46	74.30	67.69
	max	91.94	96.30	99.20	91.05	88.19	88.12	91.67	90.89
	mean	88.63	95.82	90.32	89.92	79.55	83.24	87.04	87.40
CaO (wt%)	min	1.95	0.25	0.19	1.47	0.88	0.99	1.86	1.80
	max	4.49	2.05	7.23	3.05	35.16	6.19	10.24	4.01
	mean	2.99	1.33	1.30	2.08	12.76	3.83	3.74	3.12
Al_2O_3 (wt%)	min	0.004	0.040	0.001	0.003	0.001	0.004	0.005	0.003
	max	0.822	2.584	2.404	0.505	11.188	5.339	1.890	1.248
	mean	0.107	0.419	0.233	0.043	1.186	0.577	0.287	0.092
Na_2O (wt%)	min	0.519	0.077	0.013	0.169	0.041	0.280	0.224	0.221
	max	0.982	0.542	0.602	0.374	1.725	0.499	10.985	0.439
	mean	0.665	0.284	0.118	0.250	0.509	0.401	1.137	0.351
K_2O (wt%)	min	0.076	0.028	0.016	0.169	0.012	0.207	0.167	0.185
	max	0.152	1.171	0.762	0.345	1.682	0.363	0.343	0.344
	mean	0.102	0.254	0.136	0.285	0.454	0.299	0.263	0.278
Fe_2O_3 (wt%)	min	0.111	0.023	0.016	1.366	0.143	1.447	0.768	1.574
	max	0.254	0.693	30.155	5.367	13.720	3.291	3.159	4.239
	mean	0.163	0.179	6.509	3.742	4.385	2.459	2.400	2.783
MnO	min	443.41	76.30	4.29	n.d.	35.47	n.d.	377.99	n.d.
	max	443.41	580.28	461.15	n.d.	715.31	n.d.	568.01	n.d.
	mean	443.41	174.19	79.25	–	247.67	–	473.00	–
MgO_2	min	n.d.	11.65	13.40	n.d.	4.49	n.d.	n.d.	n.d.
	max	n.d.	647.32	485.24	n.d.	739.93	n.d.	n.d.	n.d.
	mean	–	148.00	52.23	–	147.21	–	–	–
Au	min	n.d.	0.07	0.05	0.22	0.11	1.86	2.64	n.d.
	max	n.d.	0.43	142.66	38.77	209.51	1.86	47.90	n.d.
	mean	–	0.29	10.30	22.75	30.58	1.86	19.05	–
Ag	min	n.d.	0.41	0.44	36.10	0.43	n.d.	12.15	n.d.
	max	n.d.	2.10	74.75	62.85	32.17	n.d.	248.73	n.d.
	mean	–	0.85	14.96	46.34	9.30	–	111.98	–
Cu	min	n.d.	4.97	1.14	n.d.	1.35	1.17	0.54	1.18
	max	n.d.	71.95	302.96	n.d.	403.70	87.12	268.32	1.18
	mean	–	21.63	49.32	–	157.26	17.82	129.08	1.18
As	min	1240.56	38.70	503.67	8.16	16.70	10.87	6.61	7.74
	max	60189.18	472.49	24040.34	61.48	2731.66	424.95	383.72	43.62
	mean	19092.25	133.51	4233.93	20.14	662.64	102.26	60.55	18.63
Sb	min	86.82	390.95	5.34	4.78	1.42	2.33	4.11	4.14
	max	908.09	2915.75	587.74	2144.04	2305.54	12795.56	1916.34	1739.21
	mean	336.57	1007.24	274.03	339.27	394.38	1568.40	435.06	270.69
B	min	24.37	24.20	1.00	n.d.	13.76	n.d.	234.42	n.d.
	max	24.37	222.64	954.55	n.d.	645.20	n.d.	316.44	n.d.
	mean	24.37	83.45	87.85	–	196.05	–	286.06	–
Li	min	109.97	1974.01	43.78	33.30	91.65	25.29	30.41	34.74
	max	4824.89	7771.00	1916.01	519.59	3054.09	189.59	393.20	272.61
	mean	1100.36	3015.65	411.41	71.66	1213.55	91.65	84.30	101.01

quartz, and the morphological changes observed here are similar to those described in other geothermal systems (Herdianita et al., 2000a; Lynne et al., 2005; Lynne et al., 2007). These morphological changes (Figs. 4–6) are characterized by an increase in silica micro-particle abundance and variations in their size, shape and arrangement. Packed-in honeycombing (Fig. 4A), micro-botroydal clustering (Figs. 4 and 5), and sphere concatenation (Fig. 4D) causes continuous modification of the micro-surfaces and changes in the porosity of the siliceous sample. The multiple dispositions of silica micro-particles are the result of different mechanisms induced by self-assemblage and agglomeration processes, and biological activity, which control the directionality and growth of particle assembly (e.g., Jamtveit and Hammer, 2012; De Yoreo et al., 2015). The self-assemblage and biological activity are more relevant in amorphous opal A and paracrystalline opal A/CT phases (Fig. 4A, -D), while characteristics arrangements of opal CT, opal C and opal C/quartz is the result of agglomeration processes only (Fig. 4E, -D and Fig. 6). In Puchuldiza sinter deposit a complete diagenetic transition has been registered in sinter formed around hot springs with periodic activity, probably related to changes in the hydrodynamic activity of the thermal fluid source according to Guidry and Chafetz (2003).

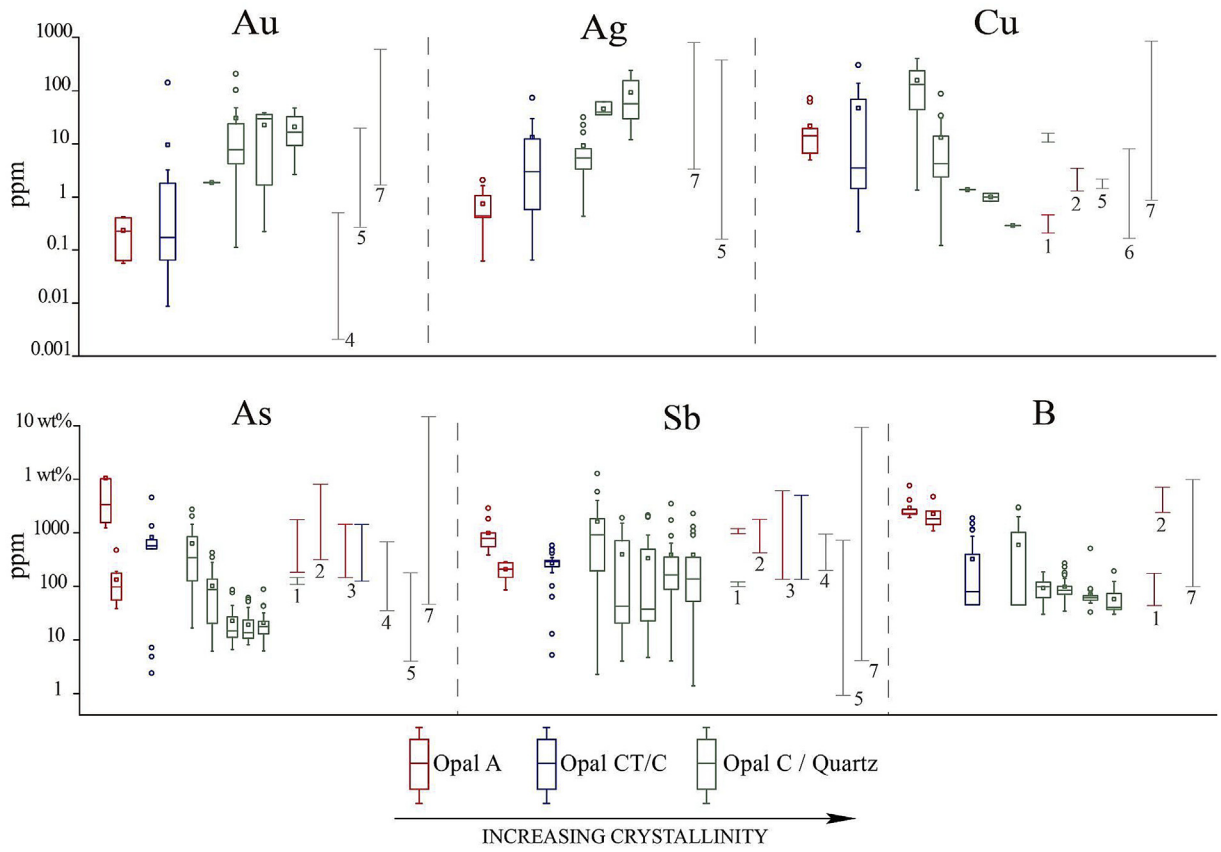

Fig. 7. Concentrations of metals and metalloids in different silica phases in sinters from Puchuldiza: Box and whisker chart showing the concentration of metals (Au, Ag, Cu) and metalloids (As, Sb, B) in sinters from Puchuldiza measured by LA-ICP-MS and plotted against the degree of crystallinity of silica. Measured concentrations in opal A, -opal CT and opal C/quartz are shown in red, blue and green boxes, respectively. As a comparison, elemental concentrations in sinters reported in the literature are shown on the right-hand side (black lines, no corresponding crystallinity data available. Red and green lines are consistent with silica phases of boxes). References: (1) Opal Mound, US (Lynne et al., 2005); (2): El Tatio, Chile (Landrum et al., 2009; Nicolau et al., 2014); (3) Steamboat Springs, US (Lynne et al., 2008); (4):Hoshino area, Japan (Belhadi et al., 2002); (5): Deseado Massif, Argentina (Guido et al., 2002); (6):Drummond Basin, Australia (Uysal et al., 2011); (7):Champagne Pool, New Zealand (Jones et al., 2001; Pope et al., 2005). (For interpretation of the references to colour in this figure legend, the reader is referred to the web version of this article.)

Table 3
Geochemistry of thermal water. The temperatures are in °C and concentrations in ppm, unless specified otherwise.

Muestra	Site 1	Site 2	Site 3	Site 4	Site 5	Site 6	Site 7	Site 11	Site 12
T	54.4	87.8	78.7	75.4	84	82.3	81.2	86	74.5
pH	6.2	8.8	7.5	7.8	8.2	8	8.3	7.4	8.2
Si	106	135	161	187	110	182	172	167	178
SiO_2	226.75	288.79	344.41	400.03	235.31	389.33	367.94	357.24	380.77
F^-	3.3	3.3	4.49	3.79	3.47	3.84	4.02	3.63	3.83
Cl^-	2389	2413	2442	2542	2316	2563	2616	2504	2519
Br^-	4.27	4.45	4.43	6.85	6.79	7.38	7.58	6.91	7.31
NO_3^-	0.88	1.04	n.d	0.79	n.d	n.d	n.d	0.62	n.d
SO_4^{2-}	131	133	134	141	125	144	143	137	148
HCO_3^-	205.01	168.4	46.37	231.86	195.25	144	154.25	118.37	231.86
Na	1425	1455	1405	1580	1425	1570	1625	1520	1570
K	144	150	183	213	176	209	218	202	211
Ca	53.7	36.8	22.5	39.7	29.9	24.4	23.1	14.5	50.6
Mg	2.32	1.42	0.46	0.99	0.84	0.57	0.64	0.23	1.08
Au (ppt)	<0.6	<0.6	<0.6	0.9	1.8	<0.6	1.3	1.6	1.6
Cu	n.d	n.d	n.d	n.d	0.0069	n.d	0.018	n.d	n.d
As	10.7	11	11.3	12.9	12.5	12.9	13	12.8	12.4
B	75.8	76.4	77.8	84.9	73.9	84.9	88.6	84.1	85.7
Sb	0.02	0.54	0.66	0.71	0.91	0.81	0.87	0.63	0.53
Hg	0.03	0.04	0.1	0.06	0.05	0.06	0.06	0.05	0.06
Li	10.9	10.7	10.6	12.6	11	12.3	12.9	12	12.4
Mn	0.66	0.22	0.072	0.14	0.12	0.015	0.016	0.024	0.21
Pb (ppb)	0.05	0.05	0.05	0.05	1.66	0.05	0.05	0.05	0.05
Sr	2.6	2.62	1.91	2.68	2.35	2.32	2.57	2.34	2.89
Cs	2.24	2.49	3.26	2.86	2.5	2.95	2.99	2.79	2.83
Ba	0.178	0.167	0.134	0.286	0.279	0.246	0.276	0.225	0.274

The geochemistry of the geothermal water and the formation of siliceous sinter are closely related, firstly by the degree of SiO_2 saturation that triggers silica precipitation, and secondly by other dissolved species and constituents in the hydrothermal fluid that may display a strong interaction with silica phases. There is consensus that the first silica phase that precipitates is opal A (Rodgers et al., 2004; Lynne et al., 2007; Orange et al., 2013), although the direct nucleation of more mature phases has been reported to occur in recent experimental studies of silica precipitation due to the variations in water chemistry (Okamoto et al., 2010; Saishu et al., 2012). Therefore, here we evaluate the potential effects of silica precipitation on the uptake of metals and metalloids, and the impact of post-depositional processes leading to trace element enrichment in the sinter.

During the first stages of sinter formation, the polymerization and subsequent coagulation/flocculation of colloidal silica particles form the amorphous opal A phase (Iler, 1979; Rimstidt and Cole, 1983; Buffle and Leppard, 1995; Herdianita et al., 2000a; Smith et al., 2003; Tobler et al., 2009; Tobler and Benning, 2013). Apart from direct co-precipitation of accessory minerals, proposed mechanisms of elemental incorporation into sinter include isomorphous substitution and chemical adsorption on the surface of silica aggregates (Ichikuni, 1970; Nelson and Giles, 1985; Saunders, 1990; Pope et al., 2005; Kaasalainen and Stefánsson, 2012). During this initial stage, silica colloids may contribute to an increase in the trace element budget throughout adsorption on silica surfaces (Buffle and Leppard, 1995; Kersting et al., 1999; De Jonge et al., 2004; Kretzschmar and Schafer, 2005). This phenomenon has been described in shallow hydrothermal systems to explain the occurrence of nanoparticles of Au and Ag (Saunders, 1990, 1994; Pope et al., 2005; Hough et al., 2011). Following adsorption of metals on silica colloids, polymerization of SiO_2 leads to the formation of opal A on preexisting surfaces such as mineral grains and even microorganisms that are exposed to recirculation of thermal water (Kersting et al., 1999; Kretzschmar and Schafer, 2005; Lynne et al., 2007; Barnard and Guo, 2012; Cademartiri et al., 2012; Alsina et al., 2013). The absence of characteristic morphologies related to other mineral phases reinforces the idea that these species are present at the nano-scale and/or covered by silica precipitates (silica microspheres or vitreous silica). Additionally, previous studies have indicated that biological agents may enhance silica precipitation and thus metal adsorption, in particular Au (Jones et al., 2001; Konhauser et al., 2001; Yokoyama et al., 2004; Lalonde et al., 2005; Pancost et al., 2005; Phoenix et al., 2005). Although microorganisms may influence metal precipitation, either as active agents during bio-mineralization or as passive agents during heterogeneous nucleation of silica, biological influences on metal uptake will not be discussed in detail here.

Environmental conditions have been reported to exert a strong influence on silica precipitation and texture development in different environmental settings (Lynne, 2012a; Nicolau et al., 2014; Campbell et al., 2015), and thus may play a role on metal uptake during the early stages of sinter formation.

The amorphous silica phases from the high-altitude Puchuldiza field (~4200 m a.s.l.) are characterized by some of the highest FWHM values reported in the literature (7–9.52 °2Θ), in agreement with previous values reported by Nicolau et al. (2014) at El Tatio (~4270 m a.s.l.). In Fig. 8, the FWHM values of high-altitude sinters from Puchuldiza and El Tatio are compared with XRD data of sinters formed under different altitude conditions worldwide. The dataset include samples from Steamboat Spring and Opal Mound, both in the US, occurring at ~1400 m a.s.l and ~1840 m a.s.l., respectively, and from the Taupo Volcanic Zone, New Zealand (Te Kopia ~410 m a.s.l, Waiotapu ~380 m a.s.l, Orakei Korako ~350 m a.s.l., and Sinter Island ~320 m a.s.l.). The representative median values of FWHM for high-altitude active sinters are above 9, while for active sinter deposits at lower altitudes FWHM values are commonly below 9. Coincidently, the highest FWHM value (12.5°2Θ) corresponds to El Tatio sinter, which is located at the highest altitude, while the lowest FWHM value (6°2Θ)

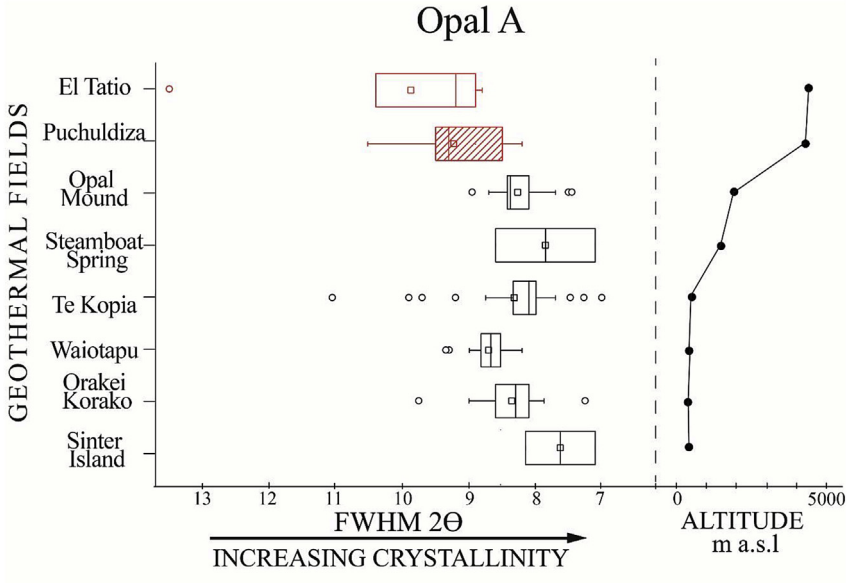

Fig. 8. Full Width Half Maximum (FWHM, or "degree of crystallinity") and topographic altitude for different sinter deposits: Box and whisker chart showing FWHM values measured on XRD traces of opal A. The data shown includes samples from Puchuldiza (this work) and from previously published studies, spanning a wide range of altitudes (m a.s.l.). The high FWHM is a key characteristic of sinter deposits from high-altitude setting (e.g., Chilean Altiplano). References: El Tatio, Chile (Nicolau et al., 2014), Opal Mound, US (Lynne et al., 2005), Steamboat Spring, US (Lynne et al., 2007), Te Kopia (Lynne and Campbell, 2004; Rodgers et al., 2004), Waiotapu, New Zealand (Lynne and Campbell, 2004; Rodgers et al., 2004), Orakei Korako, New Zealand (Lynne and Campbell, 2004) and Sinter Island, New Zealand (Lynne et al., 2007).

corresponds to Te Kopia that is located below 500 m a.s.l. High FWHM values for amorphous opal A in sinter has been attributed to: (1) Incorporation of cations attached to silanol bonds (Si-OH) in the silica network that may distort the crystalline setting (Ichikuni, 1970; Iler, 1979; Nicolau et al., 2014); (2) Incorporation of nano-minerals or mineral nano-particles within the silica matrix during the diagenesis (Garcia-Valles et al., 2008), and (3) Extreme environmental conditions typical of high-altitude systems, e.g., lower boiling point of thermal water, high evaporation rates and extreme fluctuations in daily temperatures. Therefore, the influence of these factors on silica precipitation and metal partition are yet to be explored, and further studies including laboratory and in situ precipitation experiments are needed.

Once silica is precipitated and accumulated to form sinter deposits, the diagenetic transition generate changes in the structural ordering triggering chemical diffusion processes in the silica matrix. Amorphous and para-crystalline phases have been described as open and distorted structures (e.g., opal A) that progressively order to become mature phases (Lynne and Campbell, 2004; Hinman and Walter, 2005; Lynne et al., 2007; Okamoto et al., 2010). Crystallographic defects and structural distortions of silica allow the accommodation of impurities such as (nanoscale) accessory minerals and/or ions adsorbed as cationic hydroxyl or chloride species complexes on the silica surfaces (Rossman, 1994; El-Ammouri, 2000; Veith et al., 2009; Dal Martello, 2012; Lynne, 2012b; Mohammadnejad et al., 2013). Previous studies have documented impurities in silica, including precious metals and Cu, in the form of nano-scale mineral inclusions, liquid-like inclusions and trace elements in crystalline silica phases such as quartz (e.g., Lehmann and Bambauerp, 1973; Iler, 1979; Götze et al., 2004 and references in there). During diagenesis, silica phases undergo different morphological and crystallographic modifications, including significant structural rearrangement. This process triggers the formation of structural vacancies that become available sites for diffusion of different chemical species (Dal Martello, 2012). Furthermore, cation diffusion during diagenesis may occur along grain boundaries, between phases or on the surface of micro-particles that are exposed to recirculation of thermal water, leading to fluid-mineral exchange (Dal Martello et al., 2012). Additionally, the diagenetic rate represents another factor that influences elemental mobility in sinter through retardation or acceleration of phase transitions, resulting in a modification of diffusion pathways producing a slow or fast diffusion through the silica matrix (Dal Martello et al., 2013). Therefore, a plausible mechanism to explain metal enrichment in sinter may be the result of diffusion-driven processes triggered by structural changes from opal A to quartz influenced by diagenesis. These changes would involve a crystallographic or structural refinement where, e.g., precious metals such as Au and Ag that may be present in silica as adsorbed/absorbed species or as mineral nano-particles, are later remobilized, accommodated and re-concentrated as diagenesis progresses.

5.2. Trace metal and metalloid enrichment of silica phases in sinter

Our LA-ICP-MS results indicate that the concentration of trace metals (Au, Ag, Cu) and metalloids (As, Sb, B) is correlated with the crystallinity degree of silica phases in sinter (Fig. 7). While Au and Ag are enriched in the more crystalline phases (opal C/quartz), arsenic and B concentrate preferentially in amorphous phases (opal A). These findings indicate that the diagenetic transitions of silica in sinter deposits, defined by significant structural (Fig. 3) and morphological (Figs. 4–6) changes, may play an important role on metal and metalloid enrichment in siliceous sinters and influence their budget of accessory mineral components. At Puchuldiza, samples containing amorphous opal A display the highest variability in accessory mineral occurrence; these samples contain realgar, hematite, and native sulfur, along with other detrital minerals derived from surrounding rocks such as detrital plagioclase and quartz (Fig. 3). We interpret this accessory mineral variability probably as a result of changes in the hydrogeochemistry and bio-activity present in active spring, where As, S and Fe-bearing accessory minerals co-precipitate or are induced to precipitate from metal-rich thermal waters along with opal A. In contrast, more mature sinters dominated by opal C and opal C/quartz show lower variability in their accessory mineral content; such as Hg minerals (e.g. cinnabar) that are absent from opal-A bearing samples.

We interpret the increase in concentration of Au (and Ag) in different silica phases with increased silica crystallinity as a result of post-depositional enrichment. During sinter diagenesis the continuous crystallinity and morphological changes promote the destabilization of silica surfaces by mechano-chemical processes, triggering the generation of surface defects and the creation of siloxyl ($\equiv Si-O\cdot$) and silyl ($\equiv Si\cdot$) reactive sites (or surface free radicals) (Mohammadnejad et al., 2013). These surface defects possess a high chemical activity and have been widely studied due to their high capacity to capture and favor the nucleation of metal clusters such as Au and Ag (Ferullo et al., 2006; Shor et al., 2010). The reaction below shows the formation of surface radicals by the breakage of covalent siloxane bonds after activation of the silica surface:

$$\equiv Si-O-\equiv Si \Rightarrow \equiv Si\cdot + \equiv Si-O\cdot \quad (7)$$

Mohammadnejad et al. (2013) proposed a mechanism of fixation and stabilization of Au on silica based on the interaction of silica free radicals and Au transported in the fluid. In this experimental model, the Au is transported as Au-chloride complexes in the hydrothermal fluid are electrostatically attracted to the active sites formed on the silica surface, and then chemically adsorbed on defect sites by substitution of the chloride ligand by a surface silanol. Finally, the adsorbed Au is reduced from Au^{3+} to metallic Au^0 and stabilized on the silica surface by free radical silica groups, according to:

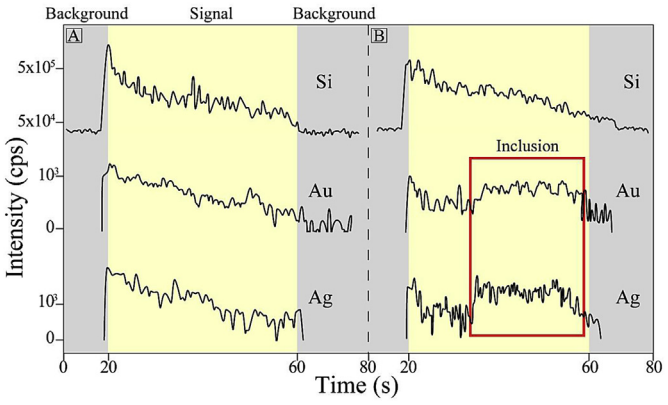

Fig. 9. Representative time vs. intensity signals for Si, Au, and Ag obtained during LA-ICP-MS analyses: The analyses correspond to sample M2.6r. (A) Profile shows homogeneous distribution of Si, Au and Ag, (B) Ablation of Au and Ag-bearing inclusions hosted in the silica matrix show as spikes in the transient signal (red rectangle). Intensity is in counts per second (cps) and time in seconds (s). (For interpretation of the references to colour in this figure legend, the reader is referred to the web version of this article.)

$$6{\equiv}Si-O\cdot + 2Au^{3+} + 3H_2O \Rightarrow 2Au^0 + 3O_2 + 6H^+ + 3{\equiv}Si-O-Si{\equiv} \quad (8)$$

$$6{\equiv}Si\cdot + 2Au^{3+} + 3H_2O \Rightarrow 2Au^0 + 6H^+ + 3{\equiv}Si-O-Si{\equiv} \quad (9)$$

Equation (8) is more suitable to describe the reduction of Au on defect sites of the silica surface, due to the lower activity of $\equiv Si-O\cdot$, which has a higher chance to react with Au-chloride complexes in comparison to $\equiv Si\cdot$, that react mainly with the environment (Mohammadnejad et al., 2013). Once Au (and Ag) are incorporated to the silica surfaces, the once dispersed nano-particles or metal clusters are embedded by silica to be later agglomerated into larger particles via Ostwald ripening during sinter diagenesis, as previously shown to support the growth of silica micro-particles in sinter formation (Rodgers et al., 2004; Wen Lou et al., 2006; Tobler et al., 2009; Mohammadnejad et al., 2013; Cassano et al., 2014). The continuous agglomeration of nano-particles of native Au (and Ag) in mature phases (opal C/quartz) causes the formation of sub-micrometer-sized inclusions of Au-Ag. Sub-micrometer-sized inclusions of native Au were detected in mature silica phases from Puchuldiza during laser ablation analysis (sample M2.6r, Fig. 9). Fig. 9A shows a LA-ICP-MS profile across a sinter grain that is representative for homogeneous or structurally-bound incorporation of Au and Ag in sinter (sample M2.6r). In contrast, the numerous spikes in the signal shown in Fig. 9B are indicative of ablation of nano-particulate inclusions of Au and Ag in sample M2.6r. Although high-resolution images of sub-micrometer-sized particles of Au (and Ag) are not presented here, similar inclusions in sinter have been previously reported and imaged by Wen Lou et al. (2006) and Cassano et al. (2014) using HR-TEM, where larger Au nanoparticles form by Ostwald ripening of smaller particles in a silica microspace (Wen Lou et al., 2006). Therefore, the highest Au and Ag concentrations detected in the more mature sinter phases (opal C/quartz in Fig. 7) at Puchuldiza are most likely related to the presence of nano-inclusions of native metals rather than structural incorporation of cationic species in quartz (Fig. 10). In quartz, trace impurities occur in vacancies, crystal defects and substitutional or interstitial positions parallel to the c-axis. However, this mineral phase has a low tolerance to incorporate foreign elements (Dal Martello, 2012). Therefore, it is likely that at least some of the Au and Ag detected in quartz in the Puchuldiza samples may reside within the crystal structure, as a result of preferential retention during diagenesis and/or late-stage diffusion (Shor et al., 2010). It is noteworthy to mention that our data show that Au and As are geochemically decoupled in sinter samples from Puchuldiza, showing opposite concentration trends with respect to silica crystallinity (Fig. 7). This geochemical behavior is different to the widely documented correspondence between Au and As that has been previously reported in pyrite and other sulfides from a wide range of hydrothermal ore deposits (Reich et al., 2005; Deditius et al., 2008, 2014 and references therein), and suggest that Au enrichment in the siliceous sinter at Puchuldiza is not controlled by As-bearing sulfide minerals.

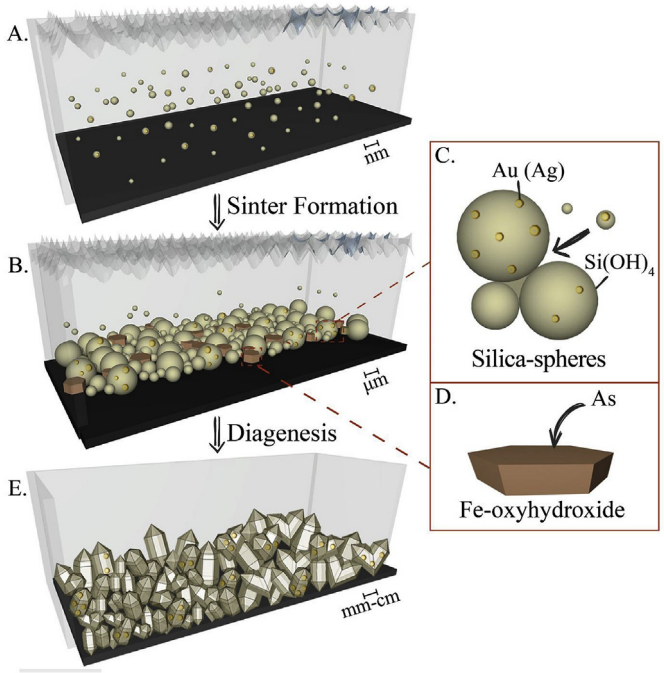

Fig. 10. Conceptual model of metal incorporation into silica phases during sinter formation: (A): At the nano-scale, the initial stage of sinter formation starts with over saturation of geothermal water with respect to silica as they discharge and cool at the surface, resulting in silica precipitation; (B): Amorphous opal A nanospheres agglomerate and form microspheres. During this stage, gold and silver are incorporated into silica spheres either as cationic species and/or metal nanoparticles or colloids (C), while arsenic and boron are incorporated into accessory minerals Fe-oxyhydroxides (D, brown). (E) As diagenesis progress, metals are enriched while metalloids are depleted from the sinter as a result of structural changes underwent by the silica host (i.e., maturation or increase in crystallinity), among other kinetically controlled processes. (For interpretation of the references to colour in this figure legend, the reader is referred to the web version of this article.)

Unlike precious metals, metalloids (As and B) show a decreasing trend with increasing crystallinity of silica (Fig. 7). The increased concentration of As in the more amorphous silica phases (opal A) is most likely related to the occurrence of As-bearing accessory minerals hosted in the sinter, i.e., realgar and Fe-oxyhydroxides (Fig. 10B, -D; Table 1). Previous studies have shown that As is preferably removed from water by adsorption on Fe-oxyhydroxides and on amorphous Fe oxides forming chemisorbed surface complexes. These processes have been reported in the El Tatio geothermal field (Zeng, 2004; Smith and Edwards, 2005; Landrum et al., 2009; Alsina et al., 2013; Nair et al., 2014; Bisone et al., 2016). The incorporation occurs only in the first step of sinter formation when the surfaces of accessory minerals are available (Fig. 10D). Post-depositional processes in sinter continuously coat the active surfaces of accessory minerals with silica, inhibiting the incorporation of As (Swedlund and Webster, 1999). Additionally, the low capacity of silica to adsorb As and its poor tolerance to hold this element within the structure contributes to the observed decrease of As concentrations in the more mature phases of silica (Smith and Edwards, 2005; Landrum et al., 2009; Nair et al., 2014). This behavior is consistent with reports by Swedlund and Webster (1999) showing that silica directly inhibits As adsorption into Fe bearing minerals at the Wairakei Geothermal Power Station, New Zealand.

It is likely that chemical species that are not enriched in the more crystalline phases (i.e., As and B) may have been lost from the silica matrix to the thermal fluid, during structural rearrangement. For example, Ichikuni (1970) proposed that B concentrations in sinter decrease during diagenesis due to crystallographic changes related to dehydration. According to the cited study, boron is incorporated into amorphous opal A by adsorption of $B(OH)^-_4$ species during silica precipitation. Further diagenetic changes would trigger B migration into the aqueous solution, leading to the observed inverse correspondence with silica crystallinity. This interpretation is in good agreement with our data where B (and also As) are preferentially enriched in the more amorphous phases (Fig. 7). This is also consistent with the fact that no B-bearing

minerals were recognized at Puchuldiza, unlike El Tatio where the arsenic borate cahnite ($Ca_4B_2As_2O_{12}{}^*4H_2O$) was reported in sinter samples (Nicolau et al., 2014).

Finally, the variable concentrations of Sb and Cu in silica, as seen in Fig. 7, are indicative that these two elements are concentrated during the first stages of silica precipitation, and do not suffer significant alterations during silica maturation. The behavior of Sb has been previously studied in the sinter deposits of El Tatio by Landrum et al. (2009), suggesting that this element partitions mainly to the opal silica matrix and co-precipitates with $Si(OH)_4$ due to the similar saturation conditions, especially as cervantite (Sb_2O_4). Variations in saturation of Sb with respect to different Sb-bearing phases such as cervantite may be the result of local temperature variations triggering the formation of silica bands enriched in nano-particles of Sb oxide minerals. In the case of Cu, its incorporation into silica phases may be similar to Au and Ag, with strong interactions due to adsorption species on to silica surfaces defects (El-Ammouri, 2000; Ferullo et al., 2006; Shor et al., 2010). However, occurrence of Cu in sinter reported here is likely related to cryptocrystalline inclusions of Cu-bearing minerals such as chrysocolla in different silica phases (Crane et al., 2001), and the low concentration could be related to its preferential co-precipitation with sulfides at the subsurface from an alkaline and boiling geothermal water (El-Ammouri, 2000; Kaasalainen and Stefánsson, 2012; Kaasalainen et al., 2015), unless there are not drillhole information available to support this hypothesis.

It is relevant to note that the precious metal and metalloid budget of sinters from Puchuldiza are within the same range of other sinter deposits worldwide (Fig. 7). In general, As, Sb, B, and Cu display high concentrations in amorphous silica phases from sinter deposits in Puchuldiza, El Tatio, Waiotapu, and Champagne Pool (Fig. 7). The amorphous opal A phase in these deposits show high to very high FWHM values, suggesting that low degrees of structural maturation generally correlated with high metalloid enrichment in sinter. In contrast, the more mature silica phases from Puchuldiza and from the Jurassic paleo-sinter of El Deseado Massif (Fig. 7) are characterized by higher concentrations of Au and Ag, although the immature silica phases at Waiotapu exhibit the same concentration range (Fig. 7). These observations suggest that, in general, mature sinter deposits host higher concentrations of precious metals such as Au and Ag, whereas metalloids such as As, Sb, and B are mainly concentrated in sinters dominated by immature phases of silica. These new finding could improve the exploration of epithermal mineral deposits.

6. Summary and concluding remarks

This work reports a comprehensive mineralogical and geochemical characterization of the metal-rich siliceous sinter deposits of Puchuldiza, in northern Chile, where the complete diagenetic sequence – i.e., amorphous opal A, paracrystalline opal A/CT, opal CT, opal C, and microcrystalline quartz – is present. The sinter deposits contain significant amounts of metals (e.g., Au, Ag, Cu) and metalloids (e.g., As, Sb, B) that are associated with different silica phases pointing to a relevant role of the degree of silica crystallinity on elemental enrichment in sinters.

Combined SEM, XRD and LA-ICP-MS data show that the concentration of metals and metalloids in sinters display a strong correspondence with silica crystallinity (Fig. 7). Arsenic and B are predominantly enriched in the more amorphous phases (opal A/CT), while Au and Ag show higher concentrations in the more crystalline phases (opal C/quartz). We interpret this differential enrichment as the result of structural, morphological and geochemical changes produced by silica maturation during sinter diagenesis.

During the first stages of sinter formation, crystallographic transition promote the generation of surface defects on silica by mechano-chemical processes, creating reactive sites where Au and Ag are electrostatically attracted and chemisorbed (Ferullo et al., 2006; Shor et al., 2010; Mohammadnejad et al., 2013). As diagenesis progresses, the generation of structural vacancies triggers the diffusion of chemical species incorporated into the less crystalline silica phases. The continuous structural changes occurring during diagenesis (Fig. 3) may promote the agglomeration of adsorbed species and embedded metal clusters through Ostwald ripening (Fig. 10), leading to the formation of nano-to micron-sized inclusions of precious metals (Fig. 9). Metalloids such as As exhibit an opposite geochemical behavior. Owing to the low capacity of silica phases to adsorb and retain arsenic, its enrichment in the more amorphous phases is most likely due to co-precipitation of As-bearing accessory minerals (e.g., realgar, orpiment) and Fe-oxyhydroxides that efficiently adsorb arsenic (Fig. 10). As a result of structural rearrangements during diagenesis, As (and B) are desorbed from the silica matrix, contributing to a progressive decrease of As in the more mature phases of silica. Finally, other enriched elements such as Sb and Cu are incorporated during in the first stages of sinter formation and their concentrations do not vary significantly during maturation, although Cu concentrations significantly decrease in the more crystalline phases.

Although these trends strongly support the role of silica crystallinity and structural maturation on metal/metalloid enrichment in sinter, further experimental and field studies are needed to fully understand the elemental partitioning behavior between silica and geothermal fluids as they discharge and cool at the surface. Among other aspects, colloidal transport of precious metals in geothermal fluids (Hannington et al., 2016), and the potential effects of microorganisms on metal fixation and nano-particle formation (Johnson et al., 2013) must be addressed. Finally, and considering the highly amorphous character of opal A in high-altitude systems such as Puchuldiza and El Tatio (Fig. 8), results from this study confirm that environmental conditions can have an unforeseen impact on silica precipitation, and thus may impact the metal/metalloid tenor of sinter deposits.

Acknowledgements

We acknowledge FONDAP-CONICYT project 15090013 “Andean Geothermal Centre of Excellence (CEGA)” for providing financial support to carry out this research, that included a M.Sc scholarship. We also acknowledge support from FONDECYT project 1130030 and FONDEQUIP EQM120098. The Millennium Nucleus for Metal Tracing Along Subduction (NMTM), MSI Grant NC130065 provided additional support to fund this study.

Appendix. Trace elements analyses determined by LA-ICP-MS. Concentration are in ppm unless specified otherwise (L.O.D.:limit of detection, n.d.:not detected, b.d.l.: below detection)

	^{29}Si	^{44}Ca	^{27}Al	^{23}Na	^{39}K	^{55}Mn	^{48}Ti	^{24}Mg	^{54}Fe	^{197}Au	^{107}Ag	^{63}Cu	^{75}As	^{121}Sb	^{7}Li	^{11}B
Error%	Reference	5.4–16.4	1–16.7	4.1–12.9	11.2–29.6	3.7–16.5	1.2–19	5.1–14.2	10.3–19	8–19.3	3.8–17.9	5.1–11.3	1.1–14.5	2–17.4	4.9–13.7	2.1–13.7
L.O.D		1240	3,88	279	39,28	2,17	2,13	1,01	280	0,07	0,26	1,11	9,86	0,9	1,93	26,32
M3.1	420189,74	16569,18	33,59	4966,45	777,28	n.d.	7,40	n.d.	925,09	n.d.	n.d.	n.d.	45909,35	201,37	n.d.	1860,99
	429000,68	17760,45	1866,31	4634,69	769,74	n.d.	24,53	n.d.	935,24	n.d.	n.d.	n.d.	1240,56	150,80	n.d.	1786,87
	427855,10	19816,95	22,22	4732,12	1137,75	343,41	11,97	n.d.	985,99	n.d.	n.d.	n.d.	10184,76	86,82	n.d.	4824,89
	429776,47	18285,65	27,10	6052,86	1150,24	n.d.	7,99	n.d.	1044,33	n.d.	n.d.	n.d.	2690,13	211,90	n.d.	2445,11
	424263,92	13930,9	298,06	7282,31	1264,05	n.d.	5,96	n.d.	778,87	n.d.	n.d.	n.d.	1559,28	262,08	24,37	2603,60
	415694,85	18318,35	94,47	5901,91	1008,54	n.d.	6,34	n.d.	1039,65	n.d.	n.d.	n.d.	3376,37	291,47	n.d.	1460,22
	412400,61	21465,93	261,23	4423,03	811,01	n.d.	5,51	n.d.	1196,77	n.d.	n.d.	n.d.	8604,76	278,39	n.d.	1109,99
	410977,50	32124,7	2066,94	5605,34	931,88	n.d.	8,15	n.d.	1775,93	n.d.	n.d.	n.d.	17001,17	294,09	n.d.	109,97
	416660,52	24458,32	4360,24	4399,24	723,72	n.d.	9,26	n.d.	1324,41	n.d.	n.d.	n.d.	35846,71	908,09	n.d.	213,88
	422252,04	21114,51	461,97	4245,33	698,47	n.d.	5,75	n.d.	1164,63	n.d.	n.d.	n.d.	22624,25	412,19	n.d.	294,82
	416873,32	26931,25	22,13	4892,52	788,93	n.d.	4,95	n.d.	1437,98	n.d.	n.d.	n.d.	11807,79	243,40	n.d.	180,27
	415859,17	19813,76	29,04	4291,71	706,74	n.d.	4,85	n.d.	1058,11	n.d.	n.d.	n.d.	8066,83	257,49	n.d.	446,90
	400256,06	25171,01	23,89	4924,98	812,01	n.d.	4,85	n.d.	1350,21	n.d.	n.d.	n.d.	11522,29	302,14	n.d.	249,37
	400300,07	21534,64	26,74	4375,37	673,69	n.d.	5,06	n.d.	1066,25	n.d.	n.d.	n.d.	60189,18	619,21	n.d.	288,54
	400256,06	20768,31	20,79	4078,60	689,75	n.d.	3,99	n.d.	1030,19	n.d.	n.d.	n.d.	17398,59	383,71	n.d.	344,60
	400253,46	25720,68	21,04	5246,69	763,61	n.d.	5,65	n.d.	1286,65	n.d.	n.d.	n.d.	21609,25	284,65	n.d.	166,70
	400240,06	19073,8	22,41	3849,99	634,66	n.d.	3,73	n.d.	930,72	n.d.	n.d.	n.d.	44936,94	533,88	n.d.	319,35
M.3.7	439171,37	10044,68	1260,21	2149,50	1324,51	67,07	10,32	48,55	n.d.	b.d.l.	0,48	6,68	38,70	390,95	30,83	2325,02
	442822,95	14255,51	1455,55	2013,80	1159,47	94,08	5,59	69,56	618,77	n.d.	0,41	6,88	63,80	491,32	44,05	2330,88
	446553,66	14647,05	686,07	2565,20	2067,81	59,10	3,70	47,26	1338,15	n.d.	n.d.	10,93	38,79	739,80	50,30	1974,01
	450076,59	6939,61	539,60	2493,51	1988,84	135,43	6,85	47,72	600,22	n.d.	n.d.	19,50	133,83	1006,17	134,94	2581,19
	450179,73	b.d.l.	691,82	972,84	562,74	82,23	6,65	35,66	n.d.	0,43	0,42	5,89	55,99	559,93	53,08	2266,16
	449690,05	1793,71	305,36	1400,81	2211,84	140,43	6,61	78,53	n.d.	n.d.	1,64	18,51	107,27	791,73	59,27	2790,62
	448482,81	n.d.	210,71	569,11	232,95	n.d.	67,33	7,02	n.d.	0,38	0,44	16,95	90,92	798,45	62,23	2282,26
	450076,59	b.d.l.	2025,90	2971,72	1481,46	150,91	42,07	109,50	894,24	n.d.	n.d.	61,48	191,13	1846,46	222,64	7771,00
	450030,59	n.d.	2370,95	2706,92	1422,26	92,69	314,89	99,71	317,96	0,07	b.d.l.	14,19	177,45	918,76	86,01	2361,42
	450068,39	b.d.l.	1199,49	1344,00	1039,45	77,70	85,41	47,88	162,35	n.d.	0,45	4,97	98,28	620,30	24,20	2299,84
	450080,59	n.d.	13708,99	4019,50	9717,72	449,41	756,76	390,38	4847,05	n.d.	2,10	71,95	472,49	2915,75	150,42	4189,74
M3.6b	370746,19	n.d.	5,90	825,80	569,00	23,96	n.d.	9,32	4286,90	0,27	n.d.	n.d.	24040,34	389,43	21,80	405,57
	377943,37	n.d.	33,15	1265,10	667,23	43,87	b.d.l.	13,77	6155,47	n.d.	n.d.	n.d.	12460,01	162,87	22,93	520,15
	328644,32	n.d.	n.d.	n.d.	3575,54	n.d.	3655,32	n.d.	210918,16	142,66	74,75	137,94	4558,53	587,74	954,55	n.d.
	344550,9	n.d.	202,59	n.d.	n.d.	n.d.	13,59	n.d.	5286,42	2,68	9,22	2,04	570,49	n.d.	b.d.l.	n.d.
	367310,26	n.d.	31,29	n.d.	1166,42	n.d.	n.d.	13,73	29230,51	n.d.	n.d.	60,15	591,73	65,21	131,40	n.d.
	365319,62	n.d.	726,45	n.d.	6324,76	248,42	210,93	18,21	n.d.	0,12	12,50	121,68	n.d.	102,97	217,62	1916,01
	418710,87	n.d.	7,47	n.d.	1429,31	357,15	n.d.	8,08	16199,17	n.d.	n.d.	120,11	1337,54	64,61	139,07	n.d.
	424048,13	51682,83	2140,41	n.d.	n.d.	53,41	402,21	292,63	n.d.	n.d.	30,29	8,57	503,67	494,06	96,77	413,79
	451411,9	8391,993	2279,38	1426,18	1164,83	68,33	374,04	63,28	n.d.	0,94	n.d.	n.d.	n.d.	424,35	23,56	101,59
	462829,79	n.d.	423,51	461,53	283,04	b.d.l.	97,55	13,39	n.d.	0,054	b.d.l.	1,88	n.d.	283,68	3,68	45,42
	462392,28	2290,2	482,90	480,82	166,57	8,72	49,91	9,97	497,38	n.d.	n.d.	1,15	n.d.	303,22	b.d.l.	46,11
	463238,71	1349,333	389,26	611,88	516,06	10,90	68,33	12,74	b.d.l.	n.d.	n.d.	1,14	b.d.l.	305,99	2,81	80,99
	463724,65	1716,927	512,28	634,43	458,22	3,32	60,47	15,12	112,74	0,15	n.d.	1,51	b.d.l.	309,51	4,01	63,93
	462274,56	b.d.l.	676,44	596,36	393,77	4,81	54,75	15,61	n.d.	0,09	n.d.	1,21	b.d.l.	279,37	2,50	70,90
	462173,67	b.d.l.	740,98	576,91	456,47	n.d.	92,55	34,19	n.d.	0,07	n.d.	3,91	n.d.	293,31	4,53	43,78
	462261,67	b.d.l.	356,26	519,09	442,40	n.d.	53,63	14,37	n.d.	b.d.l.	n.d.	b.d.l.	n.d.	280,10	2,67	77,20
	460276,21	n.d.	1434,62	97,40	115,72	n.d.	143,03	14,64	n.d.	n.d.	n.d.	n.d.	n.d.	297,03	n.d.	126,52
	425817,36	1976,856	313,19	469,09	320,23	3631	47,08	13,20	n.d.	0,23	0,58	n.d.	n.d.	294,97	1,27	47,12
	423867,91	b.d.l.	410,60	536,97	360,72	3882	53,56	21,09	n.d.	b.d.l.	n.d.	1,39	n.d.	278,62	3,98	62,91
	417301,85	4229,188	429,70	789,74	364,09	n.d.	18,17	28,33	n.d.	0,93	n.d.	3,16	n.d.	307,57	1,00	73,78
	418579,39	6751,24	12755,89	n.d.	2162,31	37,89	117,40	n.d.	163044,03	2,75	n.d.	302,96	729,82	5,34	82,87	1525,47
	448175,27	4386,816	4283,17	628,68	394,25	n.d.	99,54	11,78	n.d.	0,06	0,81	n.d.	n.d.	348,14	3,82	124,83
	448798,3	21974,3	795,79	4468,27	727,21	86,69	n.d.	36,19	n.d.	n.d.	n.d.	33,50	n.d.	477,10	n.d.	1189,09
	417301,85	n.d.	n.d.	n.d.	1060,43	22,11	66,77	n.d.	n.d.	3,25	3,79	54,72	513,50	13,18	n.d.	1155,93

(*continued on next page*)

(*continued*)

	^{29}Si	^{44}Ca	^{27}Al	^{23}Na	^{39}K	^{55}Mn	^{48}Ti	^{24}Mg	^{54}Fe	^{197}Au	^{107}Ag	^{63}Cu	^{75}As	^{121}Sb	^{7}Li	^{11}B
	417251,65	4311,617	518,23	n.d.	2398,67	n.d.	18,16	n.d.	19509,45	n.d.	2,27	77,31	523,77	237,75	36,13	n.d.
	417221,65	2144,924	252,51	484,44	211,40	4,93	3,06	10,76	n.d.	0,20	n.d.	2,75	n.d.	336,92	n.d.	80,90
	417280,55	n.d.	683,51	n.d.	n.d.	n.d.	219,21	22,53	n.d.	n.d.	0,44	n.d.	743,84	181,82	n.d.	878,99
M2.2r	417390,68	11251,96	97,39	1274,36	2770,64	n.d.	2,42	n.d.	37283,80	n.d.	n.d.	n.d.	12,72	15,22	n.d.	54,99
	417120,19	11244,8	258,53	1315,97	2819,34	n.d.	2,84	n.d.	36453,84	n.d.	n.d.	n.d.	10,16	9,64	n.d.	62,15
	416922,74	10743,11	99,51	1255,01	2515,15	n.d.	2,30	n.d.	33204,94	n.d.	n.d.	n.d.	10,78	17,93	n.d.	56,70
	417558,21	10747,26	112,04	1297,83	2560,65	n.d.	3,43	n.d.	32530,02	n.d.	n.d.	n.d.	b.d.l.	19,43	n.d.	52,08
	416247,97	12052,86	137,60	1465,30	2866,40	n.d.	2,45	n.d.	37242,49	n.d.	n.d.	n.d.	12,19	8,65	n.d.	56,77
	419172,82	12516,86	196,88	1496,20	2778,17	n.d.	2,26	n.d.	36255,80	n.d.	n.d.	n.d.	10,28	9,67	n.d.	66,11
	421715,80	10895,71	1134,51	1368,66	2489,01	n.d.	2,94	n.d.	29616,27	n.d.	n.d.	n.d.	10,25	40,50	n.d.	65,00
	422458,64	13348,82	638,61	1592,26	2732,04	n.d.	3,85	n.d.	35425,02	n.d.	n.d.	n.d.	14,44	16,01	n.d.	60,95
	423243,74	10526,47	348,67	1348,15	2339,45	n.d.	2,64	n.d.	26945,37	n.d.	n.d.	n.d.	9,99	29,90	n.d.	59,33
	422409,30	10912,05	122,55	1400,89	2263,76	n.d.	2,23	n.d.	27558,18	n.d.	n.d.	n.d.	b.d.l.	22,87	n.d.	52,96
	423206,26	11368,74	200,00	1459,80	2492,30	n.d.	5,13	n.d.	26853,28	n.d.	n.d.	n.d.	11,70	49,68	n.d.	62,82
	423795,34	13584,92	87,94	1605,42	2624,81	n.d.	4,79	n.d.	32405,23	n.d.	n.d.	n.d.	b.d.l.	26,86	n.d.	61,46
	425404,18	12548,1	86,99	1574,49	2411,88	n.d.	b.d.l.	n.d.	28801,68	n.d.	n.d.	n.d.	b.d.l.	25,59	n.d.	56,62
	424159,87	10931,74	137,08	1374,57	2202,77	n.d.	9,08	n.d.	24261,21	n.d.	n.d.	n.d.	10,88	49,44	n.d.	66,90
	422628,12	11439,48	216,94	1453,01	2161,23	n.d.	2,54	n.d.	24510,36	n.d.	n.d.	n.d.	8,39	32,80	n.d.	55,01
	420925,02	12053,93	88,52	1564,24	2498,68	n.d.	5,33	n.d.	26611,82	n.d.	n.d.	n.d.	11,47	32,37	n.d.	57,24
	417530,05	14579,9	128,69	1780,21	2596,15	n.d.	7,44	n.d.	30993,14	n.d.	n.d.	n.d.	13,10	23,05	n.d.	64,38
	417812,05	13331,47	105,73	1687,79	2437,51	n.d.	5,41	n.d.	27418,20	n.d.	n.d.	n.d.	12,26	32,20	n.d.	54,78
	418627,19	13745,07	146,79	1752,48	2506,54	n.d.	2,78	n.d.	28674,83	n.d.	n.d.	n.d.	13,86	26,94	n.d.	58,06
	417704,37	15496,62	37,99	1949,29	2692,28	n.d.	3,75	n.d.	37539,76	n.d.	n.d.	n.d.	12,54	27,79	n.d.	58,66
	418809,77	13599,02	140,20	1711,65	2330,44	n.d.	2,24	n.d.	31191,79	n.d.	n.d.	n.d.	8,16	35,64	n.d.	55,95
	420283,30	12211,06	127,70	1601,08	2091,39	n.d.	3,09	n.d.	25615,82	n.d.	n.d.	n.d.	15,89	56,50	n.d.	58,59
	417879,63	14945,33	88,17	1878,21	2512,71	n.d.	8,35	n.d.	31443,92	n.d.	n.d.	n.d.	8,44	20,05	n.d.	55,78
	417011,18	15628,76	209,07	1950,41	2537,32	n.d.	3,04	n.d.	32250,00	n.d.	n.d.	n.d.	14,67	17,49	n.d.	54,21
	416460,03	12215,73	2677,29	1594,86	2008,20	n.d.	b.d.l.	n.d.	23753,12	n.d.	n.d.	n.d.	10,67	25,46	n.d.	49,54
	414269,61	17606,17	35,11	2776,00	2747,94	n.d.	148,05	n.d.	26765,17	n.d.	n.d.	n.d.	18,36	254,45	n.d.	519,59
	413995,97	18992,49	16,24	2355,82	2702,81	n.d.	2,45	n.d.	30237,82	n.d.	n.d.	n.d.	12,22	4,78	n.d.	68,03
	414441,84	15669,32	112,47	1987,06	2232,49	n.d.	1520,51	n.d.	23151,65	n.d.	n.d.	n.d.	27,52	634,19	n.d.	78,31
	415808,36	19985,13	17,57	2422,14	2660,73	n.d.	6,25	n.d.	28618,23	n.d.	n.d.	n.d.	19,42	32,99	n.d.	74,53
	417761,97	20036,93	18,45	2447,72	2644,34	n.d.	3,76	n.d.	29061,89	n.d.	n.d.	n.d.	14,34	16,79	n.d.	50,53
	417953,82	20153,36	26,27	2519,08	2642,14	n.d.	3,64	n.d.	28318,22	n.d.	n.d.	n.d.	17,83	13,25	n.d.	55,49
	420925,25	17020,97	317,22	2176,17	2515,15	n.d.	21,08	n.d.	23467,35	n.d.	n.d.	n.d.	10,45	231,52	n.d.	87,33
	419302,28	15995,71	121,25	1981,62	2081,56	n.d.	591,40	n.d.	22017,43	n.d.	n.d.	n.d.	19,67	451,07	n.d.	62,53
	417866,36	20400,99	42,79	2466,06	2627,75	n.d.	8,25	n.d.	27777,05	n.d.	n.d.	n.d.	12,02	29,22	n.d.	69,90
	417668,34	15164,93	179,39	1887,41	2104,69	n.d.	134,03	n.d.	19856,39	n.d.	n.d.	n.d.	29,84	822,58	n.d.	88,77
	416244,29	20100,46	138,90	2469,35	2632,55	n.d.	70,76	n.d.	26834,48	n.d.	n.d.	n.d.	13,52	98,35	n.d.	81,83
	419396,44	19461,97	66,79	2413,44	2554,06	n.d.	348,80	n.d.	25396,01	n.d.	n.d.	n.d.	25,89	446,75	n.d.	91,50
	421615,37	21431,16	17,89	2597,65	2618,77	n.d.	11,23	n.d.	28033,60	n.d.	n.d.	n.d.	11,07	41,78	n.d.	60,84
	425527,91	15837,41	425,69	1934,00	2139,96	n.d.	920,04	n.d.	20380,68	n.d.	n.d.	n.d.	61,48	2144,04	n.d.	67,64
	425623,45	12314,82	615,68	1562,87	1771,37	n.d.	1222,84	n.d.	15295,89	n.d.	n.d.	n.d.	38,38	1979,53	n.d.	69,11
	424707,79	16471,86	172,41	2013,84	2120,37	n.d.	166,57	n.d.	20539,65	n.d.	n.d.	n.d.	19,33	535,68	n.d.	60,71
	425557,29	13495,54	202,64	1755,66	1975,23	n.d.	474,79	n.d.	17098,65	38,77	40,06	n.d.	53,66	922,81	n.d.	69,62
	422000,82	17633,88	247,47	2258,41	2192,12	n.d.	447,69	n.d.	21876,12	30,70		n.d.	32,35	555,26	n.d.	63,69
	423644,56	16504,26	94,38	2064,27	2072,89	n.d.	436,35	n.d.	20019,21	29,21	36,10	n.d.	40,31	525,20	n.d.	52,11
	423357,13	15008,07	211,68	1864,70	1955,89	n.d.	242,36	n.d.	17792,48	1,68	n.d.	n.d.	26,38	781,27	n.d.	64,00
	423157,39	21776,31	48,71	2645,40	2586,09	n.d.	89,20	n.d.	25934,45	n.d.	n.d.	n.d.	23,02	67,78	n.d.	64,18
	423873,70	16127,94	147,76	1953,68	2051,57	n.d.	72,45	n.d.	18672,53	n.d.	n.d.	n.d.	24,59	478,23	n.d.	69,51
	423464,17	16554,07	172,93	2031,67	2050,48	n.d.	882,15	n.d.	19043,28	n.d.	n.d.	n.d.	20,18	756,49	n.d.	72,27
	423357,13	16191,97	105,59	1966,87	1959,22	n.d.	157,77	n.d.	18248,63	n.d.	n.d.	n.d.	17,80	435,87	n.d.	60,31
	423344,23	15215,89	274,74	1862,10	1932,85	n.d.	2043,32	n.d.	17793,33	n.d.	n.d.	n.d.	56,79	2143,71	n.d.	65,99
	423320,22	14845,59	244,18	1790,95	1769,02	n.d.	1145,84	n.d.	14448,59	35,92	62,85	b.d.l.	51,90	2030,68	n.d.	67,44
	423280,22	12086,36	191,36	1333,81	1401,81	n.d.	1302,08	n.d.	9553,89	0,22	n.d.	n.d.	25,59	536,25	n.d.	33,30
M2.5	383945,42	n.d.	n.d.	n.d.	7470,80	n.d.	n.d.	n.d.	34673,94	n.d.	n.d.	297,68	b.d.l.	353,70	n.d.	1371,64

	392521,63	39190,17	576,29	1706,65	2229,39	n.d.	n.d.	5,70	6933,08	n.d.	n.d.	1,35	365,94	4,75	61,20	n.d.
	395099,21	163927,6	n.d.	n.d.	n.d.	195,54	425,09	446,22	n.d.	6,15	n.d.	159,64	1243,94	148,21	120,05	2047,13
	367163,91	46513,72	1302,33	n.d.	3126,39	n.d.	n.d.	13,82	23661,09	4,22	n.d.	n.d.	137,59	18,10	n.d.	368,28
	366486,04	n.d.	879,74	n.d.	n.d.	131,09	n.d.	23,46	12249,31	0,11	5,45	31,61	55,58	n.d.	n.d.	n.d.
	352423,67	n.d.	n.d.	3659,41	n.d.	115,30	34,14	16,47	3248,85	n.d.	n.d.	n.d.	173,46	111,25	47,81	n.d.
	361320,28	n.d.	1253,68	n.d.	n.d.	n.d.	n.d.	n.d.	n.d.	n.d.	n.d.	239,67	116,17	262,45	314,27	n.d.
	404780,48	54044,15	6033,88	8384,67	3119,86	188,48	n.d.	60,87	12791,32	n.d.	n.d.	n.d.	n.d.	82,39	189,75	n.d.
	412247,06	n.d.	7015,31	3212,28	1095,64	101,10	n.d.	15,05	n.d.	n.d.	n.d.	n.d.	327,17	n.d.	212,26	716,18
	403741,39	n.d.	n.d.	n.d.	n.d.	n.d.	76,02	21,11	n.d.	n.d.	n.d.	200,82	n.d.	n.d.	645,20	414,46
	345777,05	6253,756	3243,87	2683,31	353,39	n.d.	n.d.	31,73	1001,48	7,22	3,37	20,69	n.d.	62,94	20,09	n.d.
	333304,03	n.d.	5993,85	12794,35	6653,07	301,88	195,89	418,72	6419,26	13,27	7,76	403,70	768,90	949,82	80,20	405,83
	340959	n.d.	n.d.	5420,67	3368,34	59,20	379,93	41,18	1530,85	1,07	n.d.	n.d.	71,69	1,42	b.d.l.	n.d.
	364203,43	251289,3	59352,38	n.d.	n.d.	n.d.	n.d.	264,70	60138,42	103,21	32,17	236,1958	2041,89	9,45	533,31	2976,81
	386648,24	40185,67	3221,36	306,10	1720,85	122,83	64,93	b.d.l.	15608,43	n.d.	0,43	n.d.	n.d.	53,58	n.d.	91,65
	410745,04	n.d.	658,11	799,02	1594,35	b.d.l.	n.d.	3,73	4354,56	n.d.	n.d.	17,84	359,48	7,42	102,93	n.d.
	393537,49	n.d.	2652,26	n.d.	97,56	40,22	538,92	n.d.	n.d.	12,86778	n.d.	n.d.	658,82	1082,47	n.d.	n.d.
	362115,85	50534,03	n.d.	3853,23	3390,76	104,28	n.d.	2,70	n.d.	n.d.	8,25	n.d.	924,63	2305,54	n.d.	1597,24
	360649,56	n.d.	n.d.	6502,33	n.d.	n.d.	133,75	n.d.	n.d.	48,16	n.d.	236,46	n.d.	912,80	n.d.	3054,09
	357392,28	n.d.	1081,69	n.d.	3400,75	325,55	111,58	138,20	77379,76	10,59	3,02	100,12	n.d.	140,67	n.d.	n.d.
	365452,91	48500,32	n.d.	2232,68	n.d.	n.d.	234,12	n.d.	93261,98	7,79	22,85	56,76	n.d.	n.d.	445,14	n.d.
	384648,85	185512,1	n.d.	541,38	5395,96	553,99	n.d.	n.d.	n.d.	n.d.	n.d.	n.d.	287,54	141,46	n.d.	n.d.
	379445,86	27340,46	n.d.	n.d.	n.d.	n.d.	n.d.	n.d.	12985,83	209,51	n.d.	n.d.	16,70	n.d.	22,18	n.d.
	325333,7	n.d.	n.d.	n.d.	2620,63	27,47	n.d.	n.d.	43605,59	n.d.	5,489191	n.d.	247,22	n.d.	n.d.	170,07
	365452,91	n.d.	n.d.	n.d.	n.d.	30,56	91,37	n.d.	29555,90	n.d.	5,18	101,72	613,83	97,51	n.d.	1769,65
	365454,51	156519,5	n.d.	n.d.	13965,05	376,51	80,32	22,12	47410,85	3,48	16,63	85,51	1447,94	226,15	117,17	1382,10
	365444,61	115593,2	1095,69	736,21	n.d.	395,03	282,54	54,34	95963,70	6,76	2,91	326,48	2731,66	n.d.	13,76	n.d.
	365450,11	n.d.	7,62	n.d.	n.d.	n.d.	119,64	17,90	n.d.	24,28	7,40	n.d.	n.d.	1309,82	211,42	624,55
M2.5b	408107,54	33849,56	295,23	3454,59	2776,74	n.d.	b.d.l.	n.d.	21241,58	n.d.	n.d.	n.d.	11,68	2,51	n.d.	39,87
	408228,23	28953,46	92,80	3135,45	2576,68	n.d.	47,15	n.d.	18524,31	n.d.	n.d.	b.d.l.	20,53	281,84	n.d.	99,68
	406154,81	33396,77	45,88	3355,33	2789,67	n.d.	16,04	n.d.	20794,67	n.d.	n.d.	n.d.	22,34	66,80	n.d.	37,56
	407207,39	33564,61	22,77	3439,19	2830,20	n.d.	3,22	n.d.	21513,66	n.d.	n.d.	n.d.	b.d.l.	2,33	n.d.	31,78
	407798,34	33721,9	68,05	3363,55	2782,49	n.d.	3,28	n.d.	21085,72	n.d.	n.d.	n.d.	10,87	2,57	n.d.	31,20
	406977,79	33286,83	2545,62	3416,62	2750,69	n.d.	5,31	n.d.	20937,95	n.d.	n.d.	n.d.	12,67	12,47	n.d.	34,49
	305765,26	22755,4	193,52	2383,51	1957,11	n.d.	40,98	n.d.	14446,06	n.d.	n.d.	15,67	15,55	84,26	n.d.	53,52
	301321,56	21950,84	751,97	2482,02	2158,01	n.d.	9310,53	n.d.	15711,34	1,86	n.d.	87,12	424,95	5884,76	n.d.	112,40
	401758,38	29809,85	579,94	3089,47	2588,57	n.d.	717,87	n.d.	18277,11	n.d.	n.d.	5,07	87,53	879,09	n.d.	84,88
	403839,42	30924,7	2981,29	3182,41	2634,72	n.d.	5,57	n.d.	19154,83	n.d.	n.d.	2,74	11,19	141,84	n.d.	69,23
	404855,15	32038,4	8440,35	3301,92	2816,58	n.d.	1594,23	n.d.	19884,08	n.d.	n.d.	33,93	137,75	3401,78	n.d.	112,68
	409749,70	44246,69	567,12	3466,12	3016,78	n.d.	2,42	n.d.	15747,14	n.d.	n.d.	n.d.	b.d.l.	3,11	n.d.	30,73
	411909,74	28664,1	206,57	2348,67	2188,93	n.d.	1170,34	n.d.	10118,19	n.d.	n.d.	n.d.	92,22	930,45	n.d.	62,28
	406260,00	28992,95	313,51	2628,26	2319,04	n.d.	1398,36	n.d.	11968,05	n.d.	n.d.	n.d.	71,34	747,93	n.d.	166,14
	406469,35	28794,68	671,98	3468,70	2649,56	n.d.	1118,36	n.d.	14864,72	n.d.	n.d.	30,58	145,99	1431,87	n.d.	189,59
	403385,44	25480,63	379,78	3702,18	2199,58	n.d.	1713,03	n.d.	14268,80	n.d.	n.d.	b.d.l.	153,39	1638,87	n.d.	110,94
	400033,33	28391,38	971,97	3004,19	2732,96	n.d.	3575,75	n.d.	18403,97	n.d.	n.d.	4,24	205,63	3179,93	n.d.	122,12
	405251,53	24947,37	3830,09	2618,12	2281,49	n.d.	929,52	n.d.	14488,27	n.d.	n.d.	1,17	93,48	976,48	n.d.	152,30
	404952,34	27580,42	358,30	2956,92	2512,21	n.d.	3570,73	n.d.	17091,78	n.d.	n.d.	3,28	188,91	2388,33	n.d.	144,08
	305740,73	19821,81	426,68	2114,79	1879,28	n.d.	2838,06	n.d.	13590,16	n.d.	n.d.	2,38	125,36	1425,14	n.d.	108,38
	304529,12	19970,01	199,90	2074,26	1714,73	n.d.	470,08	n.d.	12161,87	n.d.	n.d.	n.d.	47,37	473,07	n.d.	103,36
	397723,55	24458,41	723,87	2650,68	2394,70	n.d.	963,30	n.d.	23016,61	n.d.	n.d.	n.d.	153,25	12795,56	n.d.	164,16
	395010,20	25455,73	1152,07	2696,38	2314,90	n.d.	690,41	n.d.	16152,31	n.d.	n.d.	n.d.	73,50	2003,11	n.d.	144,63
	391714,14	28084,43	28325,70	3036,69	2580,54	n.d.	479,91	n.d.	17923,36	n.d.	n.d.	13,96	68,43	1194,58	n.d.	96,53
	394593,61	31234,58	2602,36	3204,63	2619,72	n.d.	677,39	n.d.	19483,37	n.d.	n.d.	n.d.	88,87	744,10	n.d.	64,32
	394061,93	26455,74	10722,21	2906,51	2519,29	n.d.	5191,74	n.d.	17475,92	n.d.	n.d.	12,32	281,50	3510,37	n.d.	92,45
	401804,06	33634,13	7561,95	3414,93	2688,04	n.d.	955,40	n.d.	19384,16	n.d.	n.d.	n.d.	44,23	538,58	n.d.	69,27
	391714,14	28120,69	2304,68	2871,23	2556,74	n.d.	1778,16	n.d.	17581,31	n.d.	n.d.	n.d.	131,97	1856,99	n.d.	81,98
	391710,11	27764,69	10027,20	2812,69	2369,24	n.d.	1154,33	n.d.	16389,14	n.d.	n.d.	3,06	119,80	1283,22	n.d.	99,90
	391720,34	25775,67	2286,39	2796,24	2272,01	n.d.	574,76	n.d.	15420,10	n.d.	n.d.	n.d.	103,31	1137,44	n.d.	140,65
	391722,19	27103,49	5210,94	2772,58	2468,22	n.d.	713,12	n.d.	15999,29	n.d.	n.d.	b.d.l.	45,91	528,51	n.d.	106,24

(*continued on next page*)

(*continued*)

	^{29}Si	^{44}Ca	^{27}Al	^{23}Na	^{39}K	^{55}Mn	^{48}Ti	^{24}Mg	^{54}Fe	^{197}Au	^{107}Ag	^{63}Cu	^{75}As	^{121}Sb	^{7}Li	^{11}B
M2.6b	422374,63	16078,33	286,50	1938,85	1914,52	n.d.	436,01	n.d.	16580,43	n.d.	n.d.	n.d.	23,10	766,56	n.d.	80,47
	422504,35	18541,47	58,55	2302,19	2151,08	n.d.	366,06	n.d.	19476,24	9,36	67,17	n.d.	33,23	524,66	n.d.	195,31
	423552,00	16477,75	151,58	1995,76	1863,49	n.d.	2121,67	n.d.	16871,88	n.d.	n.d.	n.d.	41,83	893,16	n.d.	75,22
	426137,75	14269,81	587,52	1793,67	1750,32	n.d.	2307,97	n.d.	15004,19	n.d.	n.d.	n.d.	76,73	1916,34	n.d.	74,47
	428001,25	13426,8	554,82	1665,16	1683,72	n.d.	1416,54	n.d.	13477,57	n.d.	n.d.	n.d.	86,31	1514,99	n.d.	90,59
	427656,80	14503,36	354,15	1747,58	1733,52	n.d.	1482,42	n.d.	14534,91	n.d.	n.d.	n.d.	40,45	1232,58	n.d.	86,63
	428531,25	15533,67	271,16	1899,46	1851,31	n.d.	441,86	n.d.	15400,97	n.d.	n.d.	n.d.	27,04	777,83	n.d.	79,37
	425927,34	16746,91	189,79	1973,86	1908,62	n.d.	271,56	n.d.	16276,95	n.d.	n.d.	n.d.	19,70	712,70	n.d.	71,77
	422989,54	16874,34	113,43	2014,60	1859,31	n.d.	603,71	n.d.	16134,10	21,70	48,12	n.d.	26,46	721,67	n.d.	75,08
	419534,82	13311,6	224,76	1666,64	1564,19	n.d.	1098,96	n.d.	12655,96	47,90	248,73	n.d.	44,35	1532,53	n.d.	61,59
	417618,12	20582,89	59,20	2435,48	2167,25	n.d.	572,06	n.d.	19710,43	32,92	12,15	n.d.	36,44	570,24	n.d.	40,74
	393719,49	21081,83	67,97	2562,96	2330,93	n.d.	231,20	n.d.	20761,95	2,64	n.d.	n.d.	18,04	266,95	n.d.	126,41
	369765,16	23453,13	68,45	2627,14	2376,43	n.d.	85,09	n.d.	20119,12	n.d.	n.d.	n.d.	12,87	141,99	n.d.	75,57
	350199,63	18781,49	53,75	2036,71	1851,77	n.d.	220,66	n.d.	13392,55	11,70	n.d.	n.d.	24,16	469,04	n.d.	38,38
	347318,70	60354,43	7839,93	76471,35	1384,94	439,91	247,59	n.d.	5370,06	13,56	125,19	264,25	334,44	220,63	234,42	325,01
	371243,63	68967,03	8413,14	81491,93	1555,16	292,74	307,35	n.d.	5899,39	17,27	134,14	236,99	383,72	242,17	316,44	393,20
	396293,21	73209,37	7730,45	66602,47	1617,09	n.d.	292,61	n.d.	5478,52	14,44	148,34	268,32	335,51	249,20	307,31	243,18
	416081,95	29495,27	24,62	3246,07	2692,31	n.d.	2,95	n.d.	22097,37	n.d.	n.d.	n.d.	13,31	4,11	n.d.	30,77
	416030,25	24769,05	126,69	2701,69	2308,79	n.d.	b.d.l.	n.d.	18038,84	n.d.	n.d.	n.d.	b.d.l.	20,97	n.d.	40,65
	415188,28	23565,7	105,35	2737,37	2250,17	n.d.	2,23	n.d.	17268,60	n.d.	n.d.	n.d.	b.d.l.	36,69	n.d.	33,98
	414127,25	27914,42	158,52	3085,90	2567,90	n.d.	13,48	n.d.	20120,83	n.d.	n.d.	n.d.	16,19	43,39	n.d.	36,90
	413935,12	29748,88	62,81	3271,89	2750,16	n.d.	4,33	n.d.	21632,21	n.d.	n.d.	n.d.	11,27	15,72	n.d.	49,72
	413824,22	26530,86	157,74	3045,45	2525,24	n.d.	5,33	n.d.	19143,14	n.d.	n.d.	n.d.	14,73	28,85	n.d.	50,08
	413938,53	26324,74	61,24	2863,82	2385,87	n.d.	2,67	n.d.	18855,22	n.d.	n.d.	n.d.	12,94	13,55	n.d.	33,30
	412566,66	28203,3	228,04	3080,06	2586,28	n.d.	8,50	n.d.	20449,34	n.d.	n.d.	n.d.	14,10	21,21	n.d.	31,39
	414458,9	30137,31	73,64	3269,53	2715,98	n.d.	4,58	n.d.	21870,91	n.d.	n.d.	n.d.	11,55	6,98	n.d.	40,06
	413907,73	26732,02	115,07	2948,60	2404,96	n.d.	4,67	n.d.	18706,87	n.d.	n.d.	n.d.	13,31	35,69	n.d.	39,35
	413549,7	29623,11	38,93	3225,36	2693,54	n.d.	3,77	n.d.	21053,32	n.d.	n.d.	n.d.	6,61	14,27	n.d.	40,49
	413408,03	24009,88	281,47	2666,37	2165,91	n.d.	2,96	n.d.	17108,62	n.d.	n.d.	n.d.	11,15	21,66	n.d.	37,72
	411164,9	31782,71	234,72	3341,97	2843,74	n.d.	9,89	n.d.	21939,23	n.d.	n.d.	n.d.	b.d.l.	5,31	n.d.	38,57
	394593,61	26485,76	340,49	2800,38	2311,90	n.d.	5,81	n.d.	18136,15	n.d.	n.d.	n.d.	10,79	24,03	n.d.	35,59
	394061,93	25074,39	7704,58	2676,38	2281,77	n.d.	5,51	n.d.	16836,66	n.d.	n.d.	1,32	b.d.l.	19,14	n.d.	36,54
	401804,06	29934,62	505,32	3089,82	2555,98	n.d.	33,62	n.d.	18530,69	n.d.	n.d.	n.d.	15,59	53,29	n.d.	30,41
	413907,73	24652,9	1593,07	2482,66	2185,50	n.d.	4,06	n.d.	14334,07	n.d.	n.d.	n.d.	13,18	29,85	n.d.	33,68
	391714,14	27764,69	10027,20	2812,69	2369,24	n.d.	1154,33	n.d.	16389,14	n.d.	n.d.	3,06	119,80	1283,22	n.d.	99,90
	391702,19	25775,67	2286,39	2796,24	2272,01	n.d.	574,76	n.d.	15420,10	n.d.	n.d.	n.d.	103,31	1137,44	n.d.	140,65
	391698,24	27103,49	5210,94	2772,58	2468,22	n.d.	713,12	n.d.	15999,29	n.d.	n.d.	0,54	45,91	528,51	n.d.	106,24
M2.6r	413286,64	23425,52	260,83	2674,44	2372,25	n.d.	4,31	n.d.	20959,16	n.d.	n.d.	n.d.	22,41	172,58	n.d.	75,12
	410426,66	19134,62	749,66	2288,67	2126,09	n.d.	61,51	n.d.	16974,49	n.d.	n.d.	n.d.	21,62	130,17	n.d.	93,64
	407912,78	25593,2	6618,05	3009,00	2854,84	n.d.	106,88	n.d.	29583,90	n.d.	n.d.	n.d.	23,57	37,60	n.d.	91,48
	413534,36	26921,26	15,32	3078,04	2721,57	n.d.	2,75	n.d.	24276,94	n.d.	n.d.	n.d.	19,95	4,14	n.d.	35,92
	413345,14	27519,17	18,96	3039,05	2732,76	n.d.	2,93	n.d.	29651,91	n.d.	n.d.	n.d.	14,04	15,65	n.d.	45,25
	415842,06	23335,99	284,28	2764,22	2579,36	n.d.	18,72	n.d.	24088,86	n.d.	n.d.	n.d.	13,14	159,32	n.d.	84,49
	415778,14	18962,2	706,14	2421,18	2271,03	n.d.	5,07	n.d.	18335,75	n.d.	n.d.	1,18	18,37	276,18	n.d.	272,61
	413905,78	26768,85	154,40	3034,70	2708,88	n.d.	2,95	n.d.	25213,73	n.d.	n.d.	n.d.	11,65	29,43	n.d.	71,94
	414264,07	23679,16	29,84	2715,86	2400,42	n.d.	24,78	n.d.	22182,05	n.d.	n.d.	n.d.	18,68	611,64	n.d.	44,76
	416181,53	25083,1	40,55	2858,98	2471,05	n.d.	63,10	n.d.	22821,83	n.d.	n.d.	n.d.	11,05	191,11	n.d.	56,17
	419641,87	24358,82	66,30	2808,11	2427,36	n.d.	44,39	n.d.	22243,24	n.d.	n.d.	n.d.	14,23	191,72	n.d.	34,74
	424894,20	20073,9	77,53	2384,14	2238,35	n.d.	240,95	n.d.	17647,88	n.d.	n.d.	n.d.	18,01	605,28	n.d.	234,35
	424569,92	18358,6	70,67	2206,51	2058,71	n.d.	2,27	n.d.	16101,61	n.d.	n.d.	n.d.	b.d.l.	169,00	n.d.	176,57
	421977,30	16035,64	150,69	1958,36	1834,17	n.d.	2,37	n.d.	13932,70	n.d.	n.d.	n.d.	12,98	152,71	n.d.	183,19
	421097,05	24818,6	202,07	2866,92	2495,75	n.d.	8,77	n.d.	21619,47	n.d.	n.d.	n.d.	11,96	102,13	n.d.	86,26
	422183,82	21316,32	566,36	2497,23	2194,25	n.d.	15,13	n.d.	18701,97	n.d.	n.d.	n.d.	13,66	134,86	n.d.	85,02
	316679,66	17661,91	868,09	2102,37	1843,62	n.d.	2,29	n.d.	15213,85	n.d.	n.d.	n.d.	b.d.l.	60,02	n.d.	98,98
	317852,79	12884,94	1028,01	1637,14	1531,84	n.d.	11,16	n.d.	11009,32	n.d.	n.d.	n.d.	14,89	237,69	n.d.	190,38
	316429,04	18529,91	77,96	2021,51	1772,62	n.d.	10,50	n.d.	12979,83	n.d.	n.d.	n.d.	8,55	72,53	n.d.	82,14

421314,82	22040,63	120,79	2553,95	2191,52	n.d.	8,92	n.d.	18015,53	n.d.	n.d.	n.d.	12,77	90,18	n.d.	94,69
419754,24	21372,12	65,89	2507,03	2225,15	n.d.	4,49	n.d.	17553,62	n.d.	n.d.	n.d.	17,35	163,19	n.d.	130,97
419452,49	25361,37	392,42	2705,62	2382,26	n.d.	4,48	n.d.	17296,64	n.d.	n.d.	n.d.	13,25	101,00	n.d.	81,47
418209,02	22965,41	177,78	2649,82	2272,37	n.d.	118,30	n.d.	17923,80	n.d.	n.d.	n.d.	19,11	252,28	n.d.	69,18
418801,61	24459,62	250,28	2904,99	2448,00	n.d.	177,82	n.d.	20147,04	n.d.	n.d.	n.d.	43,62	885,32	n.d.	74,37
419750,84	21701,07	397,10	2519,95	2207,34	n.d.	116,08	n.d.	17394,68	n.d.	n.d.	n.d.	31,99	650,56	n.d.	89,70
420660,05	26479,45	52,85	2998,87	2611,37	n.d.	6,66	n.d.	21811,57	n.d.	n.d.	n.d.	15,24	60,98	n.d.	73,74
420149,10	20553,15	671,50	2915,36	2092,15	n.d.	126,94	n.d.	16823,00	n.d.	n.d.	n.d.	26,57	565,35	n.d.	78,11
417016,96	22958,62	97,97	2715,16	2329,98	n.d.	31,44	n.d.	18750,27	n.d.	n.d.	n.d.	24,42	355,94	n.d.	93,93
419750,84	17290,57	243,81	2066,24	2001,64	n.d.	785,34	n.d.	14038,77	n.d.	n.d.	n.d.	42,72	1739,21	n.d.	164,28
419757,74	27812,32	94,01	3137,99	2726,27	n.d.	3,74	n.d.	22403,93	n.d.	n.d.	n.d.	7,74	66,05	n.d.	90,69
419745,64	28671,18	36,92	3257,86	2805,90	n.d.	3,45	n.d.	23481,45	n.d.	n.d.	n.d.	19,82	20,69	n.d.	47,14
419739,44	17233,71	996,02	2096,57	1908,48	n.d.	91,01	n.d.	13760,09	n.d.	n.d.	n.d.	15,62	357,45	n.d.	101,11

References

Alsina, M.A., Zanella, L., Hoel, C., Pizarro, G.E., Gaillard, J.F., Pasten, P.A., 2013. Arsenic speciation in sinter mineralization from a hydrothermal channel of El Tatio geothermal field, Chile. J. Hydrol. 518, 434–446.

Amberg, A., 2011. NI 43-101 Technical Report, Puchuldiza Project, I Region Chile.

Aravena, D., Muñoz, M., Morata, D., Lahsen, A., Parada, M.Á., Dobson, P., 2016. Geothermics Assessment of high enthalpy geothermal resources and promising areas of Chile. Geothermics 59, 1–13.

Barbieri, R., Cavalazzi, B., Stivaletta, N., López-García, P., 2014. Silicified biota in high-altitude, geothermally-influenced ignimbrites at El Tatio geyser field, andean cordillera (Chile). Geomicrobiol. J. 31, 493–508.

Barnard, A., Guo, H., 2012. Nature's Nanostructures. Pan Standford Pte. Ltd., Singapore.

Belhadi, A., Nakanishi, T., Watanabe, K., Izawa, E., 2002. Gold mineralization and occurrence of sinter in the Hoshino area, Fukuoka prefecture. Jpn. Resour. Geol. 52, 371–380.

Benning, L.G., Phoenix, V.P., Mountain, B.W., 2005. Biosilicification: the role of cyanobacteria in silica sinter deposition. In: SGM Symp.. Micro-organisms Earth Syst., vol. 65, pp. 131–150.

Bisone, S., Chatain, V., Blanc, D., Gautier, M., Bayard, R., Sanchez, F., Gourdon, R., 2016. Geochemical characterization and modeling of arsenic behavior in a highly contaminated mining soil. Environ. Earth Sci. 75, 306.

Buffle, J., Leppard, G., 1995. Characterization of aquatic colloids and macromolecules. 1. Structure and behavior of colloidal material. Environ. Sci. Technol. 29, 2169–2175.

Cademartiri, L., Bishop, K.J.M., Snyder, P.W., Ozin, G.A., 2012. Using shape for self-assembly. Philos. Trans. R. Soc. A Math. Phys. Eng. Sci. 370, 2824–2847.

Campbell, K.A., Lynne, B.Y., Handley, K.M., Jordan, S., Farmer, J.D., Guido, D.M., Foucher, F., Turner, S., Perry, R.S., 2015. Tracing biosignature preservation of geothermally silicified microbial textures into the geological record. Astrobiology 15, 858–882.

Campbell, K., Buddle, T.F., Browne, P.R.L., 2003. Late Pleistocene siliceous sinter associated with fluvial, lacustrine, volcaniclastic and landslide deposits at Tahunaatara, Taupo Volcanic Zone, New Zealand. Earth Environ. Sci. Trans. R. Soc. Edinb. 94, 485–501.

Cassano, D., Rota Martir, D., Giovanni, S., Vincenzo, P., Violani, V., 2014. Solution phase n-doping of C60 and PCBM using tetrabutylammonium fluoride. J. Mater. Chem. 2, 303.

Crane, M.J., Sharpe, J.L., Williams, P.A., 2001. Formation of chrysocolla and secondary copper phosphates in the highly weathered supergene zones of some Australian deposits. Rec. Aust. Mus. 53, 49–56.

Dal Martello, E., 2012. Impurity Distribution and Reduction Behaviour of Quartz in the Production of High Purity Silicon. Norwegian University of Science and Technology.

Dal Martello, E., Tranell, G., Ostrovski, O., Zhang, G., Raaness, O., Larsen, R.B., Tang, K., Koshy, P., 2012. Trace elements in the Si Furnace-Part II: analysis of condensate in carbothermal reduction of quartz. Metall. Mater. Trans. B 44, 244–251.

Dal Martello, E., Tranell, G., Ostrovski, O., Zhang, G., Raaness, O., Larsen, R.B., Tang, K., Koshy, P., 2013. Trace elements in the Si Furnace-Part II: analysis of condensate in carbothermal reduction of quartz. Metall. Mater. Trans. B 44, 244–251.

Deditius, A.P., Reich, M., Kesler, S.E., Utsunomiya, S., Chryssoulis, S.L., Walshe, J., Ewing, R.C., 2014. The coupled geochemistry of Au and as in pyrite from hydrothermal ore deposits. Geochim. Cosmochim. Acta 140, 644–670.

Deditius, A.P., Utsunomiya, S., Renock, D., Ewing, R.C., Ramana, C.V., Becker, U., Kesler, S.E., 2008. A proposed new type of arsenian pyrite: composition, nanostructure and geological significance. Geochim. Cosmochim. Acta 72, 2919–2933.

El-Ammouri, E., 2000. Heavy Metals Removal from Effluents by Adsorption on Activated Silica Sols. McGill University, Montreal.

Fernandez-Turiel, J.L., Garcia-Valles, M., Gimeno-Torrente, D., Saavedra-Alonso, J., Martinez-Manent, S., 2005. The hot spring and geyser sinters of El Tatio, Northern Chile. Sediment. Geol. 180, 125–147.

Ferullo, R.M., Garda, G.R., Belelli, P.G., Branda, M.M., Castellani, N.J., 2006. Deposition of small Cu, Ag and Au particles on reduced SiO_2. J. Mol. Struct. THEOCHEM. 769, 217–223.

Fournier, R., Rowe, J., 1966. Estimation of underground temperatures from the silica content of water from hot springs and steam wells. Am. J. Sci. 264, 685–697.

Garcia-Valles, M., Fernandez-Turiel, J.L., Gimeno-Torrente, D., Saavedra-Alonso, J., Martinez-Manent, S., 2008. Mineralogical characterization of silica sinters from the El Tatio geothermal field, Chile. Am. Mineral. 93, 1373–1383.

Gibson, R.A., Sherry, A., Kaur, G., Pancost, R.D., Talbot, H.M., 2014. Bacteriohopanepolyols preserved in silica sinters from Champagne Pool (New Zealand) indicate a declining temperature gradient over the lifetime of the vent. Org. Geochem. 69, 61–69.

Gibson, R.A., Talbot, H.M., Kaur, G., Pancost, R.D., Mountain, B., 2008. Bacteriohopanepolyol signatures of cyanobacterial and methanotrophic bacterial populations recorded in a geothermal vent sinter. Org. Geochem. 39, 1020–1023.

Götze, J., Plötze, M., Graupner, T., Hallbauer, D.K., Bray, C.J., 2004. Trace element incorporation into quartz: a combined study by ICP-MS, electron spin resonance, cathodoluminescence, capillary ion analysis, and gas chromatography.

Geochim. Cosmochim. Acta 68, 3741–3759.
Guido, D., de Barrio, R., Schalamuk, I., 2002. La Marciana Jurassic sinter: implications for exploration for epithermal precious-metal deposits in Deseado Massif, southern Patagonia, Argentina. Trans. Inst. Min. Metall. Sect. B Appl. Earth Sci. 111, 106–113.
Guidry, S.A., Chafetz, H.S., 2003. Anatomy of siliceous hot springs: examples from yellowstone national park, Wyoming, USA. Sediment. Geol. 157, 71–106.
Handley, K.M., Campbell, K.A., Mountain, B.W., Browne, P.R.L., 2005. Abiotic-biotic controls on the origin and development of spicular sinter: in situ growth experiments, Champagne Pool, Waiotapu, New Zealand. Geobiology 3, 93–114.
Hannington, M., Haroardóttir, V., Garbe-Shönberg, D., Brown, K.L., 2016. Gold enrichment in active geothermal systems by accumulating colloidal suspensions. Nat. Geosci. 9, 299–302.
Herdianita, N., Brown, P., Rodgers, K., Campbell, K., 2000a. Mineralogical and textural changes accompanying ageing of silica sinter. Miner. Depos. 35, 48–62.
Herdianita, N., Rodgers, K., Browne, P.R.L., 2000b. Routine instrumental procedures to characterise the mineralogy of modern and ancient silica sinters. Geothermics 29, 65–81.
Hinman, N., Walter, M.b, 2005. Textural preservation in siliceous hot spring deposits during early diagenesis: examples from Yellowstone National Park and Nevada, U.S.A. J. Sediment. Res. 75, 200–215.
Hough, R.M., Noble, R.R.P., Reich, M., 2011. Natural gold nanoparticles. Ore Geol. Rev. 42, 55–61.
Ichikuni, M., 1970. Incorporation of siliceous and iron into siliceous sinters. Chem. Geol. 6, 273–279.
Iler, R., 1979. The Chemistry of Silica: Solubility, Polymerization, Colloid and Surface Properties, and Biochemistry.
Jamtveit, B., Hammer, Ø., 2012. Sculpting of rocks by reactive fluids. Geochem. Perspect. 1, 341–481.
JICA, 1979. Report on Geothermal Power Development Project in Puchuldiza Area. Phase I.
Johnson, C., Wyall, M., Li, X., Ibrahim, A., Schuster, J., Southam, G., Magarvey, N., 2013. Gold biomineralization by a metallophore from a gold-associated microbe. Nat. Chem. Biol. 9, 241–243.
Jones, B., Renaut, R.W., Rosen, M.R., 1999. Actively growing siliceous oncoids in the Waiotapu geothermal area, North Island, New Zealand. J. Geol. Soc. Lond. 156, 89–103.
Jones, B., Renaut, R.W., Rosen, M.R., 2001. Biogenicity of gold- and silver-bearing siliceous sinters forming in hot (75°C) anaerobic spring-waters of Champagne Pool, Waiotapu, North Island, New Zealand. J. Geol. Soc. 158, 895–911.
De Jonge, L.W., Kjaergaard, C., Moldrup, P., 2004. Colloids and colloid-facilitated transport of contaminants in soils. Vadose Zo. J. 3, 321–325.
Kaasalainen, H., Stefánsson, A., 2012. The chemistry of trace elements in surface geothermal waters and steam, Iceland. Chem. Geol. 330–331, 60–85.
Kaasalainen, H., Stefánsson, A., Giroud, N., Arnórsson, S., 2015. The geochemistry of trace elements in geothermal fluids, Iceland. Appl. Geochem. 62, 207–223. http://dx.doi.org/10.1016/j.apgeochem.2015.02.003.
Kersting, A., Efurd, D., Finnegan, D., Rokop, D., Smith, D., Thompson, J., 1999. Migration of plutonium in ground water at the Nevada Test Site. Nature 397, 56–59.
Konhauser, K.O., Jones, B., Reysenbach, A.-L., Renaut, R.W., 2003. Hot spring sinters: keys to understanding Earth's earliest life forms. Can. J. Earth Sci. 40, 1713–1724.
Konhauser, K.O., Phoenix, V.R., Bottrell, S.H., Adams, D.G., Head, I.M., 2001. Microbial-silica interactions in Icelandic hot spring sinter: possible analogues for some Precambrian siliceous stromatolites. Sedimentology 48, 415–433.
Kretzschmar, R., Schafer, T., 2005. Metal retention and transport on colloidal particles in the environment. Elements 1, 205–210.
Lahsen, A., 1970. Informe preliminar sobrelageología de Puchuldiza. CORFO- Comité Geotérmico, Estudio para el Desarrollo Geotérmico en el norte de Chile.
Lahsen, A., Sepúlveda, F., Rojas, J., Palacios, C., 2005. Present status of geothermal exploration in Chile. In: World Geothermal Congress 2005, pp. 24–29.
Lalonde, S., Konhauser, K.O., Reysenback, A., Ferris, F., 2005. The experimental silicification of Aquificales and their role in hot spring formation. Geobiology 72, 1257–1268.
Landrum, J.T., Bennett, P.C., Engel, A.S., Alsina, M.A., Pastén, P.A., Milliken, K., 2009. Partitioning geochemistry of arsenic and antimony, El Tatio geyser field, Chile. Appl. Geochem. 24, 664–676.
Lehmann, G., Bambauerp, H.U., 1973. Quartz crystals and their colors. Angew. Chem. Intern. Ed. 12, 283–291.
Liu, Y., Hu, Z., Gao, S., Günther, D., Xu, J., Gao, C., Chen, H., 2008. In situ analysis of major and trace elements of anhydrous minerals by LA-ICP-MS without applying an internal standard. Chem. Geol. 257, 34–43.
Lynne, B., Campbell, K., James, B., Browne, P., Moore, J., 2007. Tracking crystallinity in siliceous hot-spring deposits. Am. J. Sci. 307, 612–641.
Lynne, B.Y., 2012a. Life at high altitude: a comparative study of high versus low altitude hot spring settings and associated sinter textures from El Tatio, Chile and the Taupo volcanic Zone, New Zealand. Geotherm. Resour. Counc. 36, 1–7.
Lynne, B.Y., 2012b. Mapping vent to distal-apron hot spring paleo-flow pathways using siliceous sinter architecture. Geothermics 43, 3–24.
Lynne, B.Y., Campbell, K.A., 2004. Morphologic and mineralogic transitions from opal-a to opal-CT in low-temperature siliceous sinter diagenesis, Taupo volcanic Zone, New Zealand. J. Sediment. Res. 74, 561–579.
Lynne, B.Y., Campbell, K.A., Moore, J., Browne, P.R.L., 2008. Origin and evolution of the Steamboat Springs siliceous sinter deposit, Nevada, U.S.A. Sediment. Geol. 210, 111–131.
Lynne, B.Y., Campbell, K.A., Moore, J.N., Browne, P.R.L., 2005. Diagenesis of 1900-year-old siliceous sinter (opal-A to quartz) at opal Mound, Roosevelt hot springs, Utah, U.S.A. Sediment. Geol. 179, 249–278.
Mahon, W., Cusicanqui, H., 1980. Geochemistry of the Puchuldiza and Tuja hot springs, Chile. N.Z.J. Sci. 23, 149–159.
McKenzie, E.J., Brown, K.L., Cady, S.L., Campbell, K.A., 2001. Trace metal chemistry and silicification of microorganisms in geothermal sinter, Taupo Volcanic Zone, New Zealand. Geothermics 30, 483–502.
Mohammadnejad, S., Provis, J.L., Deventer, J.S.J., Van, 2013. Reduction of gold (III) chloride to gold (0) on silica surfaces. J. Colloid Interface Sci. 389, 252–259.
Nair, S., Karimzadeh, L., Merkel, B.J., 2014. Sorption of uranyl and arsenate on SiO2, Al2O3, TiO2 and FeOOH. Environ. Earth Sci. 72, 3507–3512.
Nelson, C., Giles, D., 1985. Hydrothermal eruption mechanisms and hot spring gold deposits. Econ. Geol. 80, 1633–1639.
Nicolau, C., Reich, M., Lynne, B., 2014. Physico-chemical and environmental controls on siliceous sinter formation at the high-altitude El Tatio geothermal field, Chile. J. Volcanol. Geotherm. Res. 282, 60–76.
Okamoto, A., Saishu, H., Hirano, N., Tsuchiya, N., 2010. Mineralogical and textural variation of silica minerals in hydrothermal flow-through experiments: implications for quartz vein formation. Geochim. Cosmochim. Acta 74, 3692–3706.
Orange, F., Lalonde, S.V., Konhauser, K.O., 2013. Experimental simulation of evaporation-driven silica sinter formation and microbial silicification in hot spring systems. Astrobiology 13, 163–176.
Ortiz, M., Achurra, L., Cortés, R., Fonseca, A., Silva, C., Vivallos, J., 2008. Exploración Geológica para el fomento de la energía geotérmica.
Pancost, R.D., Pressley, S., Coleman, J.M., Benning, L.G., Mountain, B.W., 2005. Lipid biomolecules in silica sinters: indicators of microbial biodiversity. Environ. Microbiol. 7, 66–77.
Parker, R.J., Nicholson, K., 1990. Arsenic in geothermal sinters: determination and implications for mineral exploration. 12th NZ Geotherm. Work. 35–39.
Phoenix, V., Renaut, R., Jones, B., Grant, F., 2005. Bacterial S-layer preservation and rare arsenic – antimony – sulphide bioimmobilization in siliceous sediments from Champagne Pool hot spring, Waiotapu, New Zealand. J. Geol. Soc. Lond. 162, 323–331.
Pope, J.G., Brown, K.L., McConchie, D.M., 2005. Gold concentrations in springs at Waiotapu, New Zealand: implications for precious metal deposition in geothermal systems. Econ. Geol. 100, 677–687.
Reich, M., Kesler, S.E., Utsunomiya, S., Palenik, C.S., Chryssoulis, S.L., Ewing, R.C., 2005. Solubility of gold in arsenian pyrite. Geochim. Cosmochim. Acta 69, 2781–2796.
Rimstidt, J., Cole, D., 1983. Geothermal mineralization I: the mechanism of formation of the Beowawe, Nevada, siliceous sinter deposit. Am. J. Sci. 283, 861–875.
Rodgers, K.A., Browne, P.R.L., Buddle, T.F., Cook, K.L., Greatrex, R. a., Hampton, W. a., Herdianita, N.R., Holland, G.R., Lynne, B.Y., Martin, R., Newton, Z., Pastars, D., Sannazarro, K.L., Teece, C. I. a, 2004. Silica phases in sinters and residues from geothermal fields of New Zealand. Earth-Sci. Rev. 66, 1–61.
Rossman, G., 1994. Colored varieties of the silica minerals. In: Heaney, P., Prewitt, C., Gibbs, G. (Eds.), Silica: Physical Behavior, Geochemistry and Materials Applications - Reviews in Mineralogy, vol. 29. Mineralogical Society of America, pp. 433–467.
Saishu, H., Okamoto, A., Tsuchiya, N., 2012. Mineralogical variation of silica induced by Al and Na in hydrothermal solutions. Am. Mineral. 97, 2060–2063.
Saunders, J.A., 1990. Colloidal transport of gold and silica in epithermal precious-metal systems: evidence from the Sleeper deposit, Nevada. Geology 18, 757–760.
Saunders, J.A., 1994. Silica and gold textures in bonanza ores of the Sleeper deposit, Humboldt County, Nevada: evidence for colloids and implications for epithermal ore-forming processes. Econ. Geol. 89, 628–638.
Schultze-Lam, S., Ferris, F.G., Konhauser, K.O., Wiese, R.G., 1995. In situ silicification of an Icelandic hot spring microbial mat: implications for microfossil formation. Can. J. Earth Sci. 32, 2021–2026.
Shor, A.M., Ivanova-Shor, E.A., Laletina, S.S., Nasluzov, V.A., Rösch, N., 2010. Small silver clusters at paramagnetic defects of silica surfaces a density functional embedded-cluster study. Surf. Sci. 604, 1705–1712.
Sillitoe, R.H., 2015. Epithermal paleosurfaces. Miner. Depos. 50, 767–793.
Smith, B., Turner, S., Rodgers, K., 2003. Opal-A and associated microbes from Wairakei, New Zealand: the first 300 days. Mineral. Mag. 563–579.
Smith, D.K., 1998. Nomenclature of the silica minerals and bibliography. Power Diffr. 13, 2–19.
Smith, S.D., Edwards, M., 2005. The influence of silica and calcium on arsenate sorption to oxide surfaces. J. Water Supply Res. Technol. - AQUA 54, 201–211.
Swedlund, P., Webster, J., 1999. Adsorption and polymerisation of silicic acid on ferrihydrite, and its effect on arsenic adsorption. Water Res. 33, 3413–3422.
Tassi, F., Aguilera, F., Darrah, T., Vaselli, O., Capaccioni, B., Poreda, R.J., Delgado Huertas, a, 2010. Fluid geochemistry of hydrothermal systems in the Arica-Parinacota, Tarapacá and Antofagasta regions (northern Chile). J. Volcanol. Geotherm. Res. 192, 1–15.
Tobler, D.J., Benning, L.G., 2013. In situ and time resolved nucleation and growth of silica nanoparticles forming under simulated geothermal conditions. Geochim. Cosmochim. Acta 114, 156–168.
Tobler, D.J., Shaw, S., Benning, L.G., 2009. Quantification of initial steps of nucleation and growth of silica nanoparticles: an in-situ SAXS and DLS study. Geochim. Cosmochim. Acta 73, 5377–5393.
Tobler, D.J., Stefánsson, A., Benning, L.G., 2008. *In-situ* grown silica sinters in

Icelandic geothermal areas. Geobiology 6, 481–502.
Uysal, I.T., Gasparon, M., Bolhar, R., Zhao, J.X., Feng, Y.X., Jones, G., 2011. Trace element composition of near-surface silica deposits-A powerful tool for detecting hydrothermal mineral and energy resources. Chem. Geol. 280, 154–169.
Veith, G.M., Lupini, A.R., Rashkeev, S., Pennycook, S.J., Mullins, D.R., Schwartz, V., Bridges, C. a., Dudney, N.J., 2009. Thermal stability and catalytic activity of gold nanoparticles supported on silica. J. Catal. 262, 92–101.
Wen Lou, X., Yuan, C., Rhoades, E., Zhang, Q., Archer, L.A., 2006. Encapsulation and Ostwald ripening of Au and Au-Cl complex nanostructures in silica shells. Adv. Funct. Mater. 16, 1679–1684.
Williams, L., Parks, G., Crerar, D., 1985. Silica diagenesis, I. Solubility controls. J. Sedment. Petrol. 89, 8463–8484.
Yokoyama, T., Taguchi, S., Motomura, Y., Watanabe, K., Nakanishi, T., Aramaki, Y., Izawa, E., 2004. The effect of aluminum on the biodeposition of silica in hot spring water: chemical state of aluminum in siliceous deposits collected along the hot spring water stream of Steep Cone hot spring in Yellowstone National Park, USA. Chem. Geol. 212, 329–337.
De Yoreo, J.J., Gilbert, P. U. P. a., Sommerdijk, N.a.J.M., Penn, R.L., Whitelam, S., Joester, D., Zhang, H., Rimer, J.D., Navrotsky, A., Banfield, J.F., Wallace, a. F., Michel, F.M., Meldrum, F.C., Colfen, H., Dove, P.M., 2015. Crystallization by particle attachment in synthetic, biogenic, and geologic environments. Science 80, 349 aaa6760.
Zeng, L., 2004. Arsenic adsorption from aqueous solutions on an Fe (III)-Si binary oxide adsorbent. Water Qual. Res. J. Can. 39, 267–275.